ACS OMEGA

http://pubs.acs.org/journal/acsodf

Article

Self-Assembled Silver Nanoparticles Decorated on Exfoliated Graphitic Carbon Nitride/Carbon Sphere Nanocomposites as a Novel Catalyst for Catalytic Reduction of Cr(VI) to Cr(III) from Wastewater and Reuse for Photocatalytic Applications

Eswaran Prabakaran[†] and Kriveshini Pillay*[,†]

Cite This: *ACS Omega* 2021, 6, 35221−35243

Read Online

ACCESS | Metrics & More | Article Recommendations | Supporting Information

ABSTRACT: Silver nanoparticles decorated on an exfoliated graphitic carbon nitride/carbon sphere (AgNP/Eg-C_3N_4/CS) nanocomposites were synthesized by an adsorption method with a self-assembled process. These nanoparticles were characterized by different techniques like UV−visible (UV−vis) spectroscopy, photoluminescence (PL) spectroscopy, Fourier transform infrared (FT-IR) spectroscopy, X-ray diffraction (XRD), thermal gravimetric analysis (TGA), Raman spectroscopy, scanning electron spectroscopy (SEM), transmission electron spectroscopy (TEM), electrochemical impedance spectroscopy (EIS), and ζ potential. AgNP/Eg-C_3N_4/CS nanocomposites showed a higher catalytic reduction activity for the conversion of Cr(VI) into Cr(III) with formic acid (FA) at 45 °C when compared to bulk graphitic carbon nitride (Bg-C_3N_4, Eg-C_3N_4, CS, and Eg-C_3N_4/CS). The kinetic rate constants were determined as a function of catalyst dosage, concentration of Cr(VI), pH, and temperature for the AgNP/Eg-C_3N_4/CS nanocomposite. This material showed higher reduction efficiency (98.5%, k = 0.0621 min^{-1}) with turnover frequency (0.0158 min^{-1}) for the reduction of Cr(VI) to Cr(III). It also showed great selectivity and high stability after six repeated cycles (98.5%). Further, the reusability of the Cr(III)-AgNP/Eg-C_3N_4/CS nanocomposite was also investigated for the photocatalytic degradation of methylene blue (MB) under visible light irradiation with various time intervals and it showed good degradation efficiency (α = 97.95%). From these results, the AgNP/Eg-C_3N_4/CS nanocomposite demonstrated higher catalytic activity, improved environmental friendliness, lower cost for the conversion of toxic Cr(VI) to Cr(III) in solutions, and also good reusability.

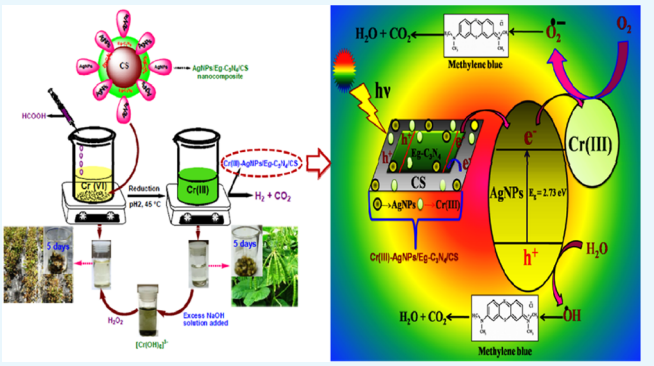

1. INTRODUCTION

Chromium(VI) is an inorganic pollutant that contaminates water and soil and produces carcinogenic and mutagenic effects in human and animals.[1−3] Most Cr(VI) is discharged into the environment by different industrial processes like metallurgy, dyeing, textiles, wood, paint, pulp, paper, leather, and metal finishing.[4−6] Chromium contains two oxidation states that are environmentally stable, and these are Cr(VI) and Cr(III), in which Cr(VI) is more toxic than Cr(III) due to better solubility and the existence of different anionic forms with pH (CrO_4^{2-}, $Cr_2O_7^{2-}$, and $HCrO_4^-$).[7,8] By contrast, Cr(III) is less toxic and inert and trace quantities are utilized in biological applications.[9] The discharge of Cr(VI) into the environment causes various diseases like cancer, skin disorders, kidney problems, vomiting, and ulcerations.[10] The World Health Organization (WHO) permitted a maximum allowable level of 0.05 mg/L for Cr(VI) in water and manages environmental release of Cr(VI).[11] Therefore, the reduction of Cr(VI) to Cr(III) with a suitable green approach and eco-friendly materials is extremely important. Various methods have been developed for the reduction of Cr(VI) to Cr(III) and include adsorption,[12] photocatalytic reduction,[13,14] electrochemical reduction,[15] ion-exchange,[16] liquid−liquid extraction,[17] biosorption,[18] electrocoagulation,[19] and precipitation.[5] These methods have however shown some disadvantages like high cost and lower concentration detection.[20,21] Hence, the researchers are significantly challenged to develop a potential environmentally conducive method. However, the catalytic reduction method has shown promise for reinforcing greater conversion of Cr(VI) to Cr(III) due to easy operation, good competence, and eco-friendliness.

Received: February 17, 2021
Accepted: April 16, 2021
Published: December 13, 2021

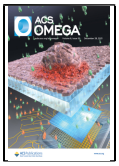

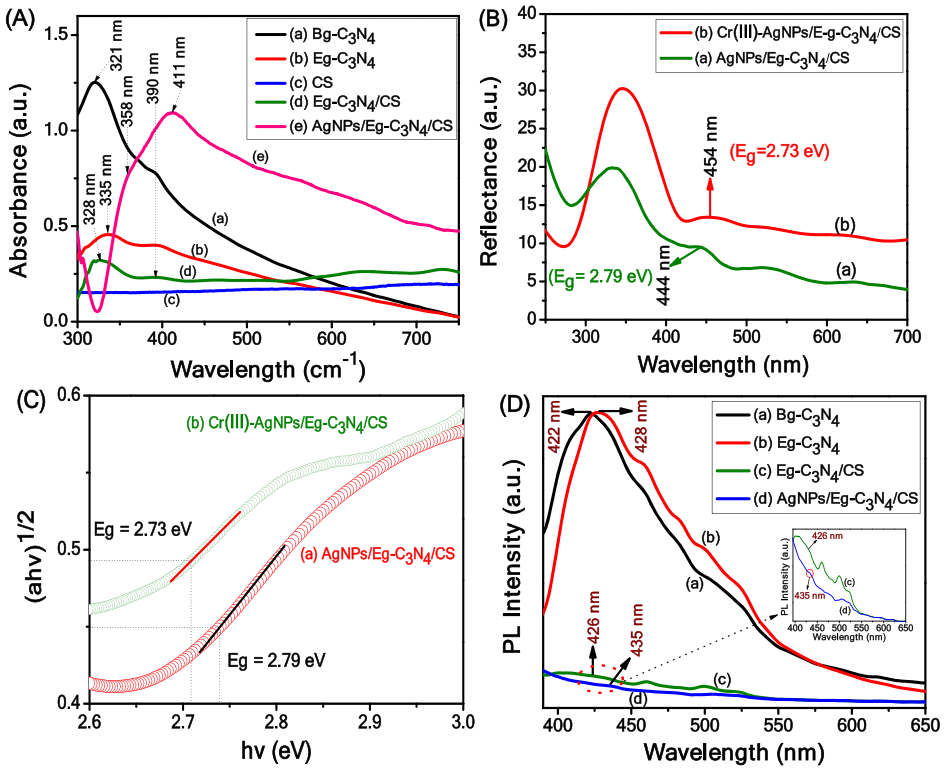

Figure 1. (A) UV−vis spectra of Bg-C_3N_4 (a), Eg-C_3N_4 (b), CS (c), Eg-C_3N_4/CS (d), and AgNP/Eg-C_3N_4/CS nanocomposites (e); (B) DRS UV−vis spectra of the AgNP/Eg-C_3N_4/CS nanocomposite (a) and Cr(III)-AgNP/Eg-C_3N_4/CS nanocomposite (b); (C) Kubelka−Munk transformation of UV−vis spectra of the AgNP/Eg-C_3N_4/CS nanocomposite and Cr(III)-AgNP/Eg-C_3N_4/CS nanocomposite; and (D) photoluminance spectra of Bg-C_3N_4 (a), Eg-C_3N_4 (b), Eg-C_3N_4/CS (c), and AgNP/Eg-C_3N_4/CS nanocomposites (d).

It is important to overcome the drawbacks associated with the catalytic reduction of Cr(VI) to Cr(III) by various materials such as H_2S, $Na_2S_2O_4$, and Fe(II).[22−24] Nowadays, noble metals (Pd, Pt, Ag, and Au),[25] noble bimetallic nanoparticles,[26,27] Pd nanoparticles,[28] core−shell AuPd@Pd nanocrystals,[29] core−shell Pd nanocrystals,[30] core−shell Pt@Pd nanowires,[31] Au@Pd heterostructures,[32] and PtAu nanospheres/reduced graphene oxide (RGO) have been utilized.[33] These nanomaterials were strongly recommended as efficient catalysts for the catalytic reduction of Cr(VI) to Cr(III).[34] However, the above materials are complicated to prepare, and consequently, their synthesis on an industrial scale is time-consuming.

Graphitic carbon nitride (g-C_3N_4) may be a metal-free catalyst with light harvesting ability for photocatalysis for the generation of hydrogen due to better conductivity of electronic transition sheet structures, physical and chemical stability, and easy availability.[35−37] However, g-C_3N_4 has demonstrated lower catalytic activity because of a higher electron−hole recombination rate with light absorption, less density of active sites, low electrical conductivity, and a high wavelength region.[38−40] Additionally, g-C_3N_4 with carbon materials possessed enhanced properties such as mechanical strength, electrical conductivity, and thermal stability.[41,42] The composite materials of carbon@g-C_3N_4, carbon dots/g-C_3N_4, graphene/g-C_3N_4, and carbon nanotube (CNT)/g-C_3N_4 have enhanced properties like conductivity, hydrogenation evolution, and photo-electrochemical activity.[43−46] Among them, carbon@g-C_3N_4 composite material has shown high surface area, good stability in physicochemical processes, low electron−hole recombination rate, good electronic transition in band structure, and better visible (vis) light photocatalyst activity.

Different nanocomposites such as Pd/graphene oxide (GO),[47] Pd@granular activated carbons (GACs),[48] Pd-CNTs,[49] Ni@C-dots,[50] Ag−Au/RGO,[51] Ni@GR-Cu,[52] Pd@SiO_2−NH_2,[53] polyaniline (PANI)/MnO_2/TiO_2,[54] Pt/Pd nanoparticles,[55] palladium (Pd) tetrapods,[56] AgCl@Ag/CS−NCs,[57] Ag/SnO_2/NiO,[58] CdS/RGO,[59] g-C_3N_4/$ZnFe_2O_4$,[60] Fe_3O_4/RGO,[61] CuO/ZrO_2-MCM-4,[62] α-MnO_2@RGO,[63] G-Fe_3O_4 and Au/G-Fe_3O_4,[64] α-FeOOH nanorod/RGO,[65] $Gd(OH)_3$ nanorod/RGO,[66] p−n heterojunction of $MCeO_2$−$BiFeO_3$,[67] Bi/Bi_2MoO_6,[68] and Ag@Ag_3PO_4/g-C_3N_4/NiFe layered double hydroxide (LDH)[69] have been used for the photocatalytic and catalytic reduction of Cr(VI) to Cr(III). Nowadays, formic acid (FA, HCOOH) is used in the reduction of Cr(VI) to Cr(III) and it acts as a reducing agent for the generation of hydrogen and carbon dioxide during the reaction.[70] Generally, the noble metals (Ag, Au, Pd, Pt, etc.) are coated on a hybrid composite to enhance the catalytic activity and reduce the electron−hole recombination rate and they have shown surface plasmon resonance (SPR) for charged electrons to hybrid composites and hydrogen production for the reduction of Cr(VI) to Cr(III).[58,71,72] Among these, Ag showed low toxicity, high surface area, better optical and electrical conductivities, and low band gap energy when compared to those of Pt and Pd.[73−75]

Herein, for the first time, the preparation of a novel silver nanoparticles decorated on exfoliated graphitic carbon nitride/carbon spheres (AgNP/Eg-C_3N_4/CS) nanocomposite has been reported and used for the catalytic reduction of Cr(VI) to Cr(III). Various precursors of melamine and D-dextrose were used for the synthesis of bulk graphitic carbon nitride (Bg-C_3N_4) and carbon sphere (CS) using thermal and hydrothermal methods, respectively. The exfoliated graphitic carbon nitride

https://doi.org/10.1021/acsomega.1c00866
ACS Omega 2021, 6, 35221−35243

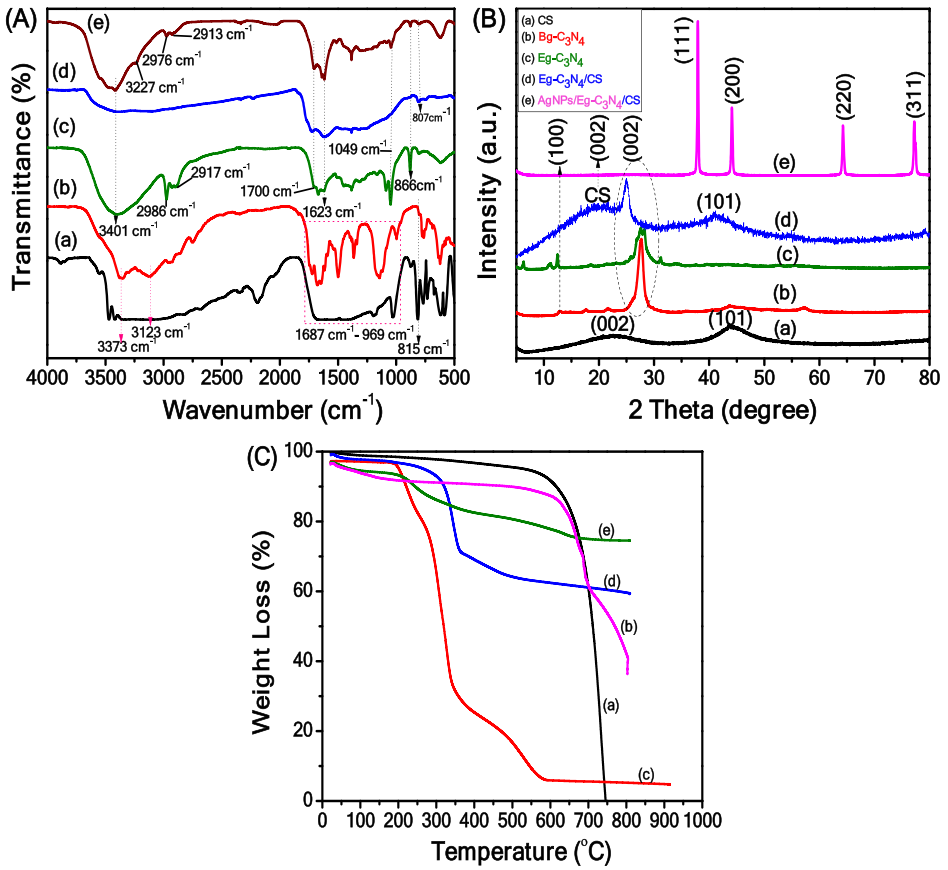

Figure 2. (A) FT-IR spectra of Bg-C_3N_4 (a), Eg-C_3N_4 (b), CS (c), Eg-C_3N_4/CS (d), and AgNP/Eg-C_3N_4/CS nanocomposites (e); (B) X-ray diffraction (XRD) spectra of Bg-C_3N_4 (a), Eg-C_3N_4 (b), CS (c), Eg-C_3N_4/CS (d), and AgNP/Eg-C_3N_4/CS nanocomposites (e); and (C) thermal gravimetric analysis (TGA) spectra of Bg-C_3N_4 (a), Eg-C_3N_4 (b), CS (c), Eg-C_3N_4/CS (d), and AgNP/Eg-C_3N_4/CS nanocomposites (e).

(Eg-C_3N_4) was prepared by an ultrasonication method with H_2SO_4 treatment. The preparation of the Eg-C_3N_4/CS composite was synthesized by an adsorption method. To the best of our knowledge, there are no reports on the AgNPs coated on the Eg-C_3N_4/CS nanocomposite. This nanocomposite was therefore employed in a chemical reduction method with $NaBH_4$ as a reducing agent. This AgNP/Eg-C_3N_4/CS nanocomposite was characterized by various instrumental methods and used for the catalytic reduction of Cr(VI) to Cr(III) in water with formic acid as a reducing agent at 45 °C. Thereafter, the reuse application for the photocatalytic degradation of methylene blue (MB) was conducted with the Cr(III)-AgNP/Eg-C_3N_4/CS nanocomposite after reduction under visible light irradiation with various time intervals.

2. RESULTS AND DISCUSSION

2.1. Detailed Mechanism Formation of Self-Assembled AgNP/Eg-C_3N_4/CS Nanocomposites. An adsorption method was described for the synthesis of AgNP/Eg-C_3N_4/CS nanocomposite photocatalysts, and the preparation method is explained, as shown in Scheme 3. First, g-C_3N_4 was obtained by a thermal polycondensation method with melamine and it was dispersed in sulfuric acid with sonication to get Eg-C_3N_4. Then, CS was added into the mixture, which is obtained from D-dextrose by a hydrothermal method. The CS was coated on Eg-C_3N_4 to form a Eg-C_3N_4/CS composite due to electrostatic attraction between the negative charge of CS and positive charge of Eg-C_3N_4. Then, the addition of $AgNO_3$ and sodium borohydrate (reducing agent) provided electrons for the formation of AgNPs from the $AgNO_3$ solution to form the AgNP/Eg-C_3N_4/CS nanocomposite under stirring conditions.[76] Finally, the mixture was centrifuged to remove impurities and water and dried at room temperature to obtain the AgNP/Eg-C_3N_4/CS nanocomposite. In this method, Eg-C_3N_4 and CS were used as materials to form the self-assembled nanocomposite and they hindered the aggregation of AgNPs. Finally, the AgNP/Eg-C_3N_4/CS nanocomposite has shown good photocatalytic activity.

2.2. Characterization. *2.2.1. UV−Visible Spectroscopy Study.* Figure 1A(a−e) shows the UV−visible spectra of Bg-C_3N_4, Eg-C_3N_4, CS, Eg-C_3N_4/CS, and AgNP/Eg-C_3N_4/CS nanocomposites in the solution state. The spectrum of Bg-C_3N_4 showed peaks at 321 and 390 nm,corresponding to n−π^* and π−π^* of C═N in the triazine group.[77,78] The spectrum of Eg-C_3N_4 showed a shift to higher wavelength at 335 nm (π−π^*) with a lower intensity peak at 390 nm (n−π^*) when compared to that of Bg-C_3N_4, and this change was due to single-layer protonation of Eg-C_3N_4 with acid treatment, as shown in Figure 1A(b).[79,80] Bare CS does not show any distinct absorption peaks, as shown in Figure 1A(c). Figure 1A(d) shows that the peak moved to a blue shift at 328 nm (π−π^*) and there was a minimized peak intensity at 390 nm (n−π^*) due to sp^2 hybridization of Eg-C_3N_4, which contributed to greater absorption of light and also lowered the band gap energy.[41,81] Figure 1A(e) shows two peaks at 411 and 358 nm, which corresponded to surface plasmon resonance (SPR) of AgNPs and electronic transitions in Eg-C_3N_4 groups during the self-assembly formation of the AgNP/Eg-C_3N_4/CS nanocompo-

https://doi.org/10.1021/acsomega.1c00866
ACS Omega 2021, 6, 35221−35243

site.[82] Figure 1B(a,b) shows the UV−visible diffuse reflectance spectra, which were used to calculate the band gap energy before and after reduction of Cr(VI) with the AgNP/Eg-C_3N_4/CS nanocomposite. Figure 1B(a) shows a peak at 444 nm due to the SPR effect of AgNPs in the AgNP/Eg-C_3N_4/CS nanocomposite.[83] The Cr(III)-AgNP/Eg-C_3N_4/CS nanocomposite showed a slightly red shift with reduced peak intensity at 454 nm, which confirmed the successful reduction Cr(VI) to Cr(III) and Cr(III) coating on the AgNP/Eg-C_3N_4/CS nanocomposite, as shown in Figure 1B(b). The band gap energies of the AgNP/Eg-C_3N_4/CS nanocomposite (2.79 eV) and Cr(III)-AgNP/Eg-C_3N_4/CS nanocomposite (2.73 eV) were obtained by the Kubelka−Munk plot of band gap energy (eV) vs $(\alpha h\nu)^{1/2}$, as shown in Figure 1C(a,b). Therefore, lower band gap energy also confirmed the effective reduction of Cr(VI) to Cr(III) with the AgNP/Eg-C_3N_4/CS nanocomposite.

2.2.2. Photoluminescence (PL) Study. The photoluminescence (PL) spectrum was used to determine the charge separation efficiency of photogenerated electrons and holes in catalyst materials.[84] Figure 1D(a−d) shows that the PL spectra of Bg-C_3N_4, Eg-C_3N_4, Eg-C_3N_4/CS, and AgNP/Eg-C_3N_4/CS nanocomposites were measured with the recombination of electron and holes. The PL spectra of Bg-C_3N_4 showed a high-intensity peak at 422 nm, while the excitation wavelength was 360 nm, which shows additionally high recombination of electron−hole pairs, as shown in Figure 1D(a). Eg-C_3N_4 increased the peak intensity and slightly shifted the peak position at 428 nm at an excitation wavelength of 360 nm, and it also displayed the highest recombination of electron−hole pairs. By comparison of AgNP/Eg-C_3N_4/CS with Eg-C_3N_4/CS, the peak intensity for the AgNP/Eg-C_3N_4/CS nanocomposite decreased when compared to that of Eg-C_3N_4/CS. This is due to the fact that the AgNPs self-assembled on Eg-C_3N_4/CS lowered the recombination rate of electron−hole charge carriers, as shown in Figure 1D(d) (inset).[85] The reduced recombination rate of photogenerated electron−hole pairs was due to the higher catalytic activity when compared to Eg-C_3N_4/CS, Eg-C_3N_4, and Bg-C_3N_4. In this study, CS was negligible for PL analysis.

2.2.3. Fourier Transform Infrared (FT-IR) Study. The FT-IR spectra of Bg-C_3N_4, Eg-C_3N_4, CS, Eg-C_3N_4/CS, and AgNP/Eg-C_3N_4/CS nanocomposites were recorded to identify functional groups in the as-prepared materials, as shown in Figure 2A(a−e). Figure 2A(a) shows that the spectrum of Bg-C_3N_4 has several peaks at around 1687−969 cm^{-1}, which corresponded to C═N, C−N, and C−NH−C stretching vibrations of tri-*s*-triazine molecules.[86,87] A sharp peak at 815 cm^{-1} was recorded and ascribed to the out-of-plane bending vibration of triazine units.[64] Two broad peaks were noted at 3373 and 3123 cm^{-1}, and these are attributed to the N−H stretching vibration of the amine group and O−H stretching vibrations of water molecules on the Bg-C_3N_4 surface.[88] Figure 2A(b) shows that the sulfuric acid treatment of the Eg-C_3N_4 sheet also resulted in a peak with increasing intensity of the broad region of N−H amine and O−H stretching vibration and tri-*s*-triazine units of C−N and C−NH−C stretching vibration groups.[89] The triazine unit showed reduced peak intensity at 815 cm^{-1}, which confirmed the acidification of Eg-C_3N_4, as shown in Figure 2A(b). CS shows a broad peak with high intensity at 3401 cm^{-1}, which appeared due to the O−H stretching vibration. Peaks at 2986 and 2917 cm^{-1} were assigned to the C−H stretching vibration of sp^2 (═CH_2) and sp^3 (−CH_3) hybridization, respectively. The bands at 1700 and 1623 cm^{-1} were denoted by the C═O and C═C stretching vibrations, respectively, which implied the aromatization of D-dextrose.[90] The bands at 1049 and 866 cm^{-1} indicated the C−OH and C−H bending vibrations, respectively, which contained a OH group and an aromatic moiety on the CS, as shown in Figure 2A(c). Eg-C_3N_4/CS of N−H, O−H, C═O, and C═C groups showed decreased peak intensity, and the peaks associated with C−H and C−OH disappeared without a change in position, as shown in Figure 2A(d). The triazine unit was shifted to a lower wavenumber at 807 cm^{-1}, and it is evident that Eg-C_3N_4 was enclosed on CS.[43,91,92] Figure 2A(e) shows that the majority of the peaks were mostly increased because AgNPs self-assembled on Eg-C_3N_4/CS as a result of electrostatic forces between AgNPs and Eg-C_3N_4/CS nanocomposites.[82,93]

2.2.4. XRD Study. The XRD pattern was used to determine the crystalline and amorphous nature of Bg-C_3N_4, Eg-C_3N_4, CS, Eg-C_3N_4/CS, and AgNP/Eg-C_3N_4/CS nanocomposites, as shown in Figure 2B(a−e). Bg-C_3N_4 showed two diffraction peaks at 13.06 and 27.77°, which corresponded to (100) and (002) planes, and these were related to diffraction planes of Bg-C_3N_4 (JCPDS Card no. 46-1088),[94] as shown in Figure 2B(b). The high-intensity peak of the (002) plane was dependent on interlayer stacking in the aromatic structure of graphite materials.[95] The low-intensity peak of the (100) plane was based on the in-planar repeating motifs of the tri-*s*-triazine unit.[96] Eg-C_3N_4 showed a changed peak position with low-intensity peaks at 12.43 and 27.55°, as shown in Figure 2B(c). Figure 2B(a) shows that two peaks were observed at 2θ = 23.15 and 44.58° for CS and were attributed to (002) and (101) planes, respectively, with a hexagonal graphite lattice structure. These diffraction patterns were correlated to CS (JCPDS no. 75-1621).[36] Figure 2B(d) shows that Eg-C_3N_4/CS exhibited a broad and sharp peaks at 25.01 and 19.36°, which were assigned to the (002) plane of CS and (002) plane of Eg-C_3N_4.[97] This XRD spectrum unambiguously confirmed that Eg-C_3N_4 was self-assembled on CS. The AgNP/Eg-C_3N_4/CS nanocomposite showed several diffraction peaks at 37.95, 44.08, 64.27, and 77.33°, which are related to the (111), (200), (220), and (311) planes of the FCC structure of AgNPs, respectively.[98−100] These were correlated with JCPDS card no. 01-089-3722 of AgNPs. The other diffraction peaks of CS (002) and Eg-C_3N_4 (002) disappeared due to the strong self-assembly of AgNPs on the Eg-C_3N_4/CS nanocomposite, as shown in Figure 2B(e). The mean crystallite size D_{hkl} was calculated using the predominant peak related to the AgNPs at 37.95° along the (111) plane and Scherrer's formula $D = K\lambda/(B\cos\theta)$ (where K = 0.9 is a dimensionless shape factor, λ(CuKR) = 0.15418 nm, θ is the Bragg angle, and B is the full width at half-maximum of the diffraction peak, in radian); the average grain size of the AgNPs is calculated to be about D = 10 nm based on the observable four crystal directions and is consistent with the transmission electron spectroscopy (TEM) observations.

2.2.5. TGA Study. Thermal stabilities of Bg-C_3N_4, Eg-C_3N_4, CS, and Eg-C_3N_4/CS and AgNP/Eg-C_3N_4/CS nanocomposites were determined by thermogravimetric analysis, as shown in Figure 2C(a−e). Bg-C_3N_4 showed a weight loss at 550−750 °C, which means that the decomposition of carbon nitride occurred with 63.67% weight loss, as shown in Figure 2C(a).[101,102] Figure 2C(b) shows that Eg-C_3N_4 exhibited two weight losses at 500−710 °C (29.6%) and 95−250 °C (2.67%) corresponding to the removal of carbon nitride and water molecules, respectively. As can be seen from the spectra, Eg-C_3N_4 showed less weight loss than Bg-C_3N_4 due to high thermal stability of Eg-C_3N_4.[103] CS showed three curves at the 25−125 °C, 125−378 °C, and 378−

https://doi.org/10.1021/acsomega.1c00866
ACS Omega 2021, 6, 35221−35243

690 °C temperature ranges, which corresponded to weight losses of 1.6, 27.67, and 8.83%, respectively, as shown in Figure 2C(c). The first curve was formed due to elimination of moisture, the second curve was due to the decomposition of oxygen groups, and the third curve was due to the dehydration of oxygen-containing groups on CS. Eg-C_3N_4/CS showed a clear bending curve at 95−225 °C, which was based on the elimination of water, another weight loss at 225−375 °C, which was attributed to the decomposition of CS, and the last bending curve at 375−650 °C, which was due to the decomposition of carbon nitride in Eg-C_3N_4, as shown in Figure 2C(d). The AgNP/Eg-C_3N_4/CS nanocomposite showed large curves at 115−335 °C with 10.06% weight loss and at 375−725 °C with 7.94% weight loss, as shown in Figure 2C(e). From the results, the self-assembled AgNP/Eg-C_3N_4/CS nanocomposite showed higher thermal stability than Eg-C_3N_4/CS, CS, Eg-C_3N_4, and Bg-C_3N_4.[104]

2.2.6. Raman Study. Raman spectra were recorded to investigate the crystalline nature of carbon materials of Bg-C_3N_4, Eg-C_3N_4, CS, Eg-C_3N_4/CS, and AgNP/Eg-C_3N_4/CS nanocomposites, as shown in Figure S1A−E, Supporting Information. Figure 3A shows two bands, which appeared at 1445 and

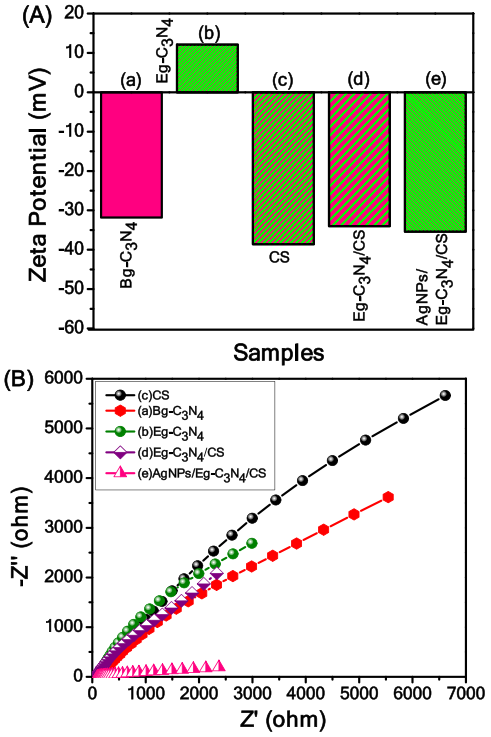

Figure 3. (A) ζ potentials of (a) Bg-C_3N_4, (b) Eg-C_3N_4, (c) CS, (d) Eg-C_3N_4/CS, and (e) AgNP/Eg-C_3N_4/CS nanocomposites and (B) electrochemical impedance spectroscopy (EIS) Nyquist plot of (a) Bg-C_3N_4, (b) Eg-C_3N_4, (c) CS, (d) Eg-C_3N_4/CS, and (e) AgNP/Eg-C_3N_4/CS nanocomposites.

1556 cm^{-1} and corresponded to the D-band and G-band of amorphous Bg-C_3N_4 atoms, respectively.[105] The D-band represented the disordered phase and defects of the graphite layer of sp^3 atoms in ring modes of the A1 symmetry, and the G-band was attributed to the graphite structure of the E_{2g} mode of sp^2 carbon−carbon bonds atoms in the ring and chains.[106] The peaks at 577, 785, and 1115 cm^{-1} corresponded to the A1′ vibration symmetry of tri-*s*-triazine units of Bg-C_3N_4.[107,108] The peaks at 673 and 978 cm^{-1} were assigned to the 2 mode and 1 mode of traizine rings of Bg-C_3N_4 atoms, respectively, as shown in Figure S1A, Supporting Information.[109] The tri-*s*-triazine units of Eg-C_3N_4 showed both high-intensity and low-intensity peaks at 547 and 1115 cm^{-1}, respectively, and the peak at 651 cm^{-1} together with some other peaks disappeared. The peaks of triazine units reduced in intensity as well and the peak positions changed to 651 and 993 cm^{-1}, respectively, which confirmed that Eg-C_3N_4 contained sulfuric acid. The D-band and G-band also decreased in peak intensity at 1458 and 1551 cm^{-1}, respectively, as shown in Figure S1B, Supporting Information. The ratio of I_D/I_G showed the defects and disorders in the graphite material. The I_D/I_G value of Eg-C_3N_4 (1.04) was higher than that of Bg-C_3N_4 (0.98), which provided evidence that the structure of Eg-C_3N_4 was more disordered and contained more defects.[110] The Raman spectra of CS, Eg-C_3N_4/CS, and AgNP/Eg-C_3N_4/CS nanocomposites showed the two important vibrations of the D-band and G-band, as shown in Figure S1C−E, Supporting Information. The comparison of I_D/I_G ratio values for CS (1.07), Eg-C_3N_4/CS (1.01), and AgNP/Eg-C_3N_4/CS nanocomposite (0.96) showed that the AgNP/Eg-C_3N_4/CS nancomposite contained less disorder in its structure when compared to Bg-C_3N_4, Eg-C_3N_4, Eg-C_3N_4/CS, and CS.[111,112] As can be seen from Figure S1A−E, Supporting Information, the I_D/I_G value of the AgNP/Eg-C_3N_4/CS nanocomposite was lowered, which means that the AgNPs preferred the degree of graphite carbon atoms.[113,114]

2.2.7. Brunauer−Emmett−Teller (BET) Study. The surface area, pore volume, and pore size were observed by the Brunauer−Emmett−Teller (BET) method with nitrogen adsorption−desorption processes.[115] Figure S2A−E (Supporting Information) shows the surface areas of Bg-C_3N_4, Eg-C_3N_4, CS, Eg-C_3N_4/CS, and AgNP/C_3N_4/CS nanocomposites, which were determined by isothermal N_2 adsorption−desorption BET methods at 10 °C/min.[116−119] These obeyed the type H3 hysteresis loop model and also assumed mesoporous and macroporous properties by Barrett−Joyner−Halenda (BJH) plots with pore size distribution range 10−100 nm, as shown in Figure S2A−E (inset), Supporting Information. Among them, the AgNP/Eg-C_3N_4/CS nanocomposite showed the higher surface area and lower size because of electrostatic attractions between AgNPs and Eg-C_3N_4/CS nanocomposites, which were favored for catalytic applications.

2.2.8. Analysis. The surface charge of self-assembly processes was also investigated by ζ potential measurements. The surface charges of Bg-C_3N_4, Eg-C_3N_4, CS, and Eg-C_3N_4/CS and AgNP/Eg-C_3N_4/CS nanocomposites were measured. The ζ potentials corresponded to −31.8, 12.1, −38.6, −34.0, and −35.4 mV, respectively, as shown in Figure 3A(a−e). Bg-C_3N_4 indicated a negative charge ζ potential at −31.8 mV due to the amine groups of heptazine rings.[120] The ζ potential of Eg-C_3N_4 showed a positive potential at 12.1 mV, which is due to the protonation of Eg-C_3N_4 with H_2SO_4. CS displayed a higher negative charge potential at −38.6 mV due to the several oxygen atoms of COOH and OH groups. After self-assembly of Eg-C_3N_4/CS, a less negative potential at −34.0 mV was noted when compared to the potential of CS because of the positive charge of Eg-C_3N_4 coated on the negative charge of CS with electrostatic interactions.[121,122] The AgNP/Eg-C_3N_4/CS nanocomposite also increased the negative charge to about −35.4 mV due to electrostatic repulsion forces between AgNPs and the Eg-C_3N_4/CS nanocomposite.[123]

2.2.9. EIS Study. Electrochemical impedance spectroscopy (EIS) measurement was used to determine the electron-transfer

https://doi.org/10.1021/acsomega.1c00866
ACS Omega 2021, 6, 35221−35243

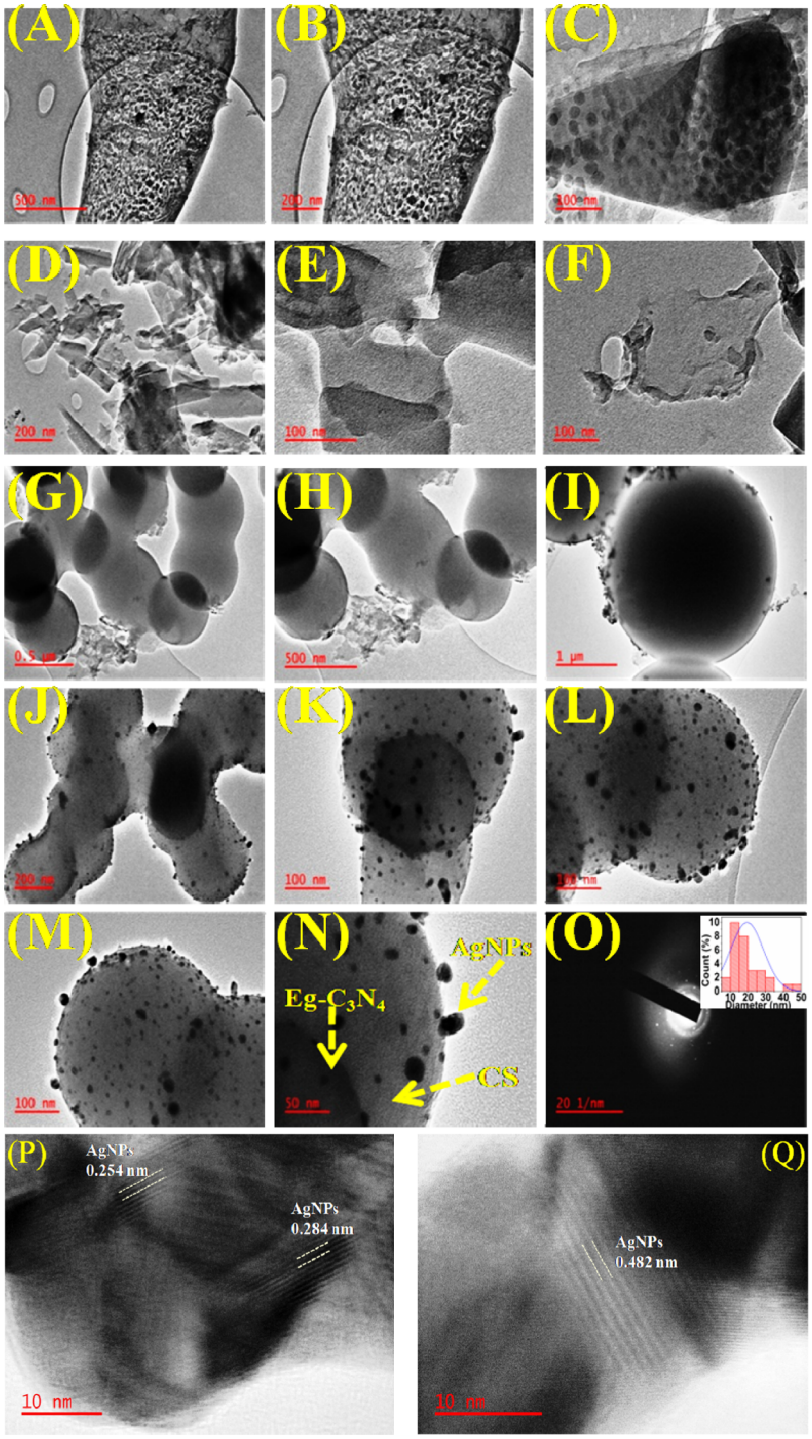

Figure 4. TEM images of Bg-C_3N_4 at (A) 500 nm, (B) 200 nm, and (C) 100 nm; Eg-C_3N_4 at (D) 200 nm, (E) 100 nm, and (F) 100 nm; Eg-C_3N_4/CS at (G) 0.5 μm, (H) 500 nm, and (I) 1 μm; AgNP/Eg-C_3N_4/CS nanocomposite at (J) 200 nm, (K) 100 nm, (L) 100 nm, (M) 100 nm, and (N) 50 nm. (O) SAED pattern of the AgNP/Eg-C_3N_4/CS nanocomposite (inset: histogram of the particle size distribution). (P, Q) High-resolution TEM images of AgNPs on the AgNP/Eg-C_3N_4/CS nanocomposite.

behavior of the catalyst. The radius of the arc is related to the charge-transfer behavior at the electrode−electrolyte interface.[124] The conductivity behavior and resistance of Bg-C_3N_4, Eg-C_3N_4, CS, Eg-C_3N_4/CS, and AgNP/Eg-C_3N_4/CS nanocomposites were modified on a glassy carbon electrode (GCE) in a supporting electrolyte solution of 0.1 M KCl and 10 mM $K_3[Fe(CN)_6]^{3-/4-}$ with a frequency range of 0.1−100 kHz, as shown in Figure 3B(a−e). The EIS Nyquist plot of CS spheres showed a large arc radius due to less charge separation and low electron transfer at the electrode and electrolyte interface, as shown in Figure 3B(c). Bg-C_3N_4 exhibited higher resistance and lower conductivity because of a large semicircle arch, which blocks the electron transfer, as shown in Figure 3B(a).[125] The semicircle arch was slightly decreased and also the conductivity slightly increased with reduced resistance of Eg-C_3N_4, as shown in Figure 3B(c).[126] Eg-C_3N_4/CS was also reduced in diameter due to Eg-C_3N_4 self-assembled on CS, which increased the conductivity and improved the electron transfer, as shown in

https://doi.org/10.1021/acsomega.1c00866
ACS Omega 2021, 6, 35221−35243

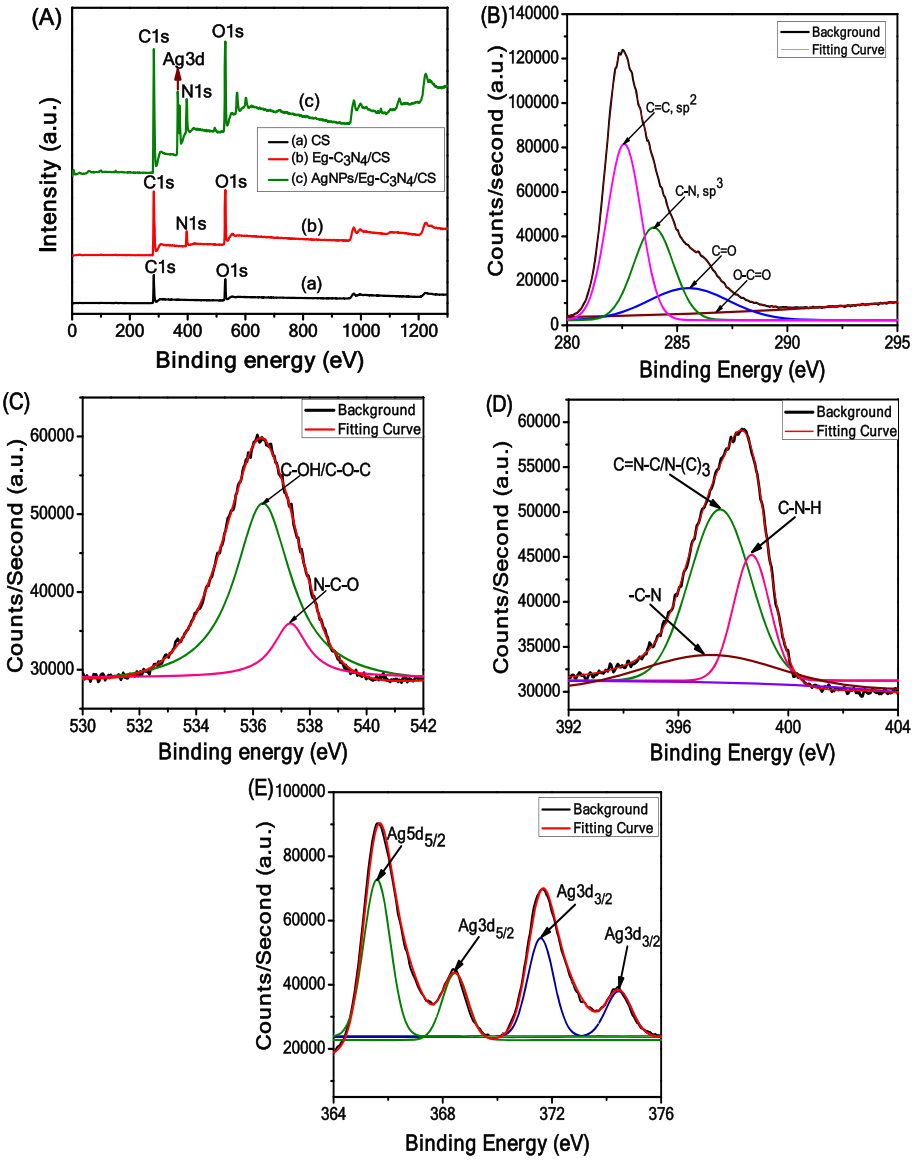

Figure 5. (A) XPS survey spectra of CS (a), Eg-C_3N_4/CS (b), and AgNP/Eg-C_3N_4/CS nanocomposite (c) and fitting curves of (B) C 1s, (C) O 1s, (D) N 1s, and (E) Ag 3d and Ag 5d of the AgNP/Eg-C_3N_4/CS nanocomposite.

Figure 3B(d).[127] The AgNP/Eg-C_3N_4/CS nanocomposite semicircle of the Nyquist plot showed a smaller arc because of AgNPs hindering the recombination of electron−hole charge separation toward the catalytic reduction of Cr(VI) to Cr(III), as shown in Figure 3B(e). The AgNP/Eg-C_3N_4/CS nanocomposite catalyst conducted the charge transfer between the modified electrode and electrolyte solution more effectively than Eg-C_3N_4/CS, CS, Eg-C_3N_4, and Bg-C_3N_4.[128]

2.2.10. Surface Morphology Study. The surface morphologies of Bg-C_3N_4, Eg-C_3N_4, CS, Eg-C_3N_4/CS, and AgNP/Eg-C_3N_4/CS nanocomposites was determined by scanning electron spectroscopy (SEM), as shown in Figure S3A−E, Supporting Information. The image of multilayer with aggregated sheets of Bg-C_3N_4 was displayed at a high magnification of 10 μm, as shown in Figure S3A, Supporting Information. Eg-C_3N_4 showed several single-layer sheets at 10 μm magnification, which confirmed that Eg-C_3N_4 was acid-treated. Bg-C_3N_4 is shown in Figure S3B, Supporting Information. The uniform spherical shape was observed at a high magnification of 2 μm, which is due to the carbonization of D-dextrose to CS, as shown in Figure S3C, Supporting Information. Eg-C_3N_4 was coated on the smooth surface of CS. Eg-C_3N_4/CS at magnification of 2 μm is shown by the yellow arrow shown in Figure S3D, Supporting Information. The white particles of AgNPs coated on the Eg-C_3N_4/CS composite (AgNP/Eg-C_3N_4/CS nanocomposite) at 2 μm are shown in Figure S3E, Supporting Information, which is formed by the electrostatic interaction between the AgNPs and Eg-C_3N_4/CS. The chemical composition of the AgNP/Eg-C_3N_4/CS nanocomposite presented C, N, O, and Ag, and they were evaluated by energy-dispersive X-ray analysis (EDAX), as shown in Figure S3F, Supporting Information.

2.2.11. TEM Study. The TEM images further confirmed the sizes and shapes of Bg-C_3N_4, Eg-C_3N_4, CS, Eg-C_3N_4/CS, and AgNP/Eg-C_3N_4/CS nanocomposites, as shown in Figure 4A−N. The Bg-C_3N_4 showed sheetlike structures with black dots at various magnifications of 500, 200, and 100 nm, as shown in Figure 4A−C. At a high magnification of 100 nm, Bg-C_3N_4 revealed multilayer sheets, as shown in Figure 4C. The single-layer sheets with dispersed images were displayed at 200, 100 and 100 nm magnifications, as shown in Figure 4D−F. Figure 4F

https://doi.org/10.1021/acsomega.1c00866
ACS Omega 2021, 6, 35221−35243

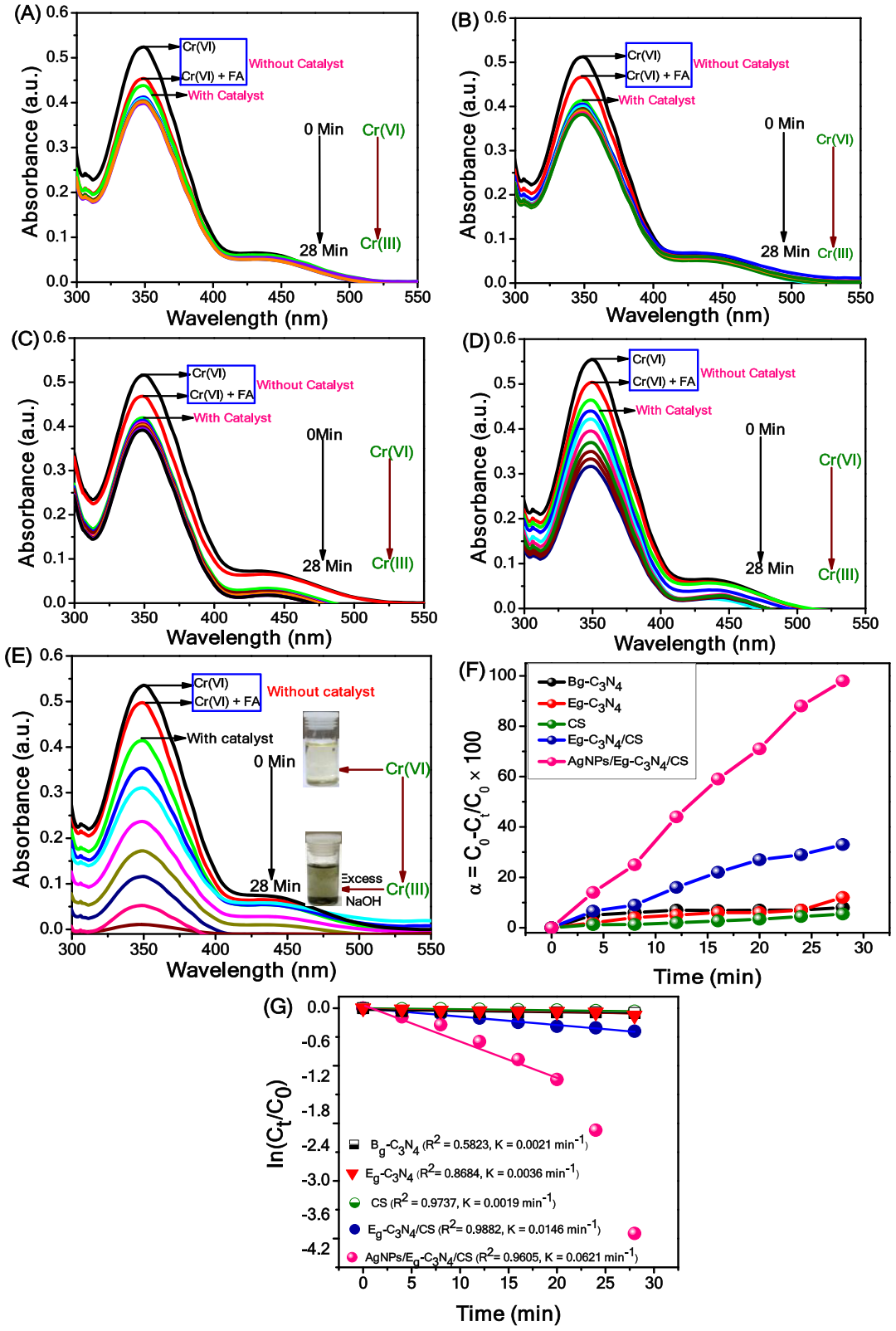

Figure 6. UV−vis spectra for catalytic reduction of Cr(VI) to Cr(III) in FA with different catalysts: 15 mg/mL (A) Bg-C_3N_4, (B) Eg-C_3N_4, (C) CS, (D) Eg-C_3N_4/CS, and (E) AgNP/Eg-C_3N_4/CS nanocomposite for 0−28 min at 45 °C and pH 2; (F) plot of the reduction efficiency % vs time; and (G) plot of $\ln(C_t/C_0)$ vs time of Bg-C_3N_4, Eg-C_3N_4, CS, Eg-C_3N_4/CS, and AgNP/Eg-C_3N_4/CS nanocomposites. Digital images of additional excess of 10 M NaOH to green precipitate of $Cr(OH)_6^{3-}$ ((E) inset).

shows that a clear single sheet was recorded at 100 nm magnification, which confirmed the formation of Eg-C_3N_4 with ultrasonication. Eg-C_3N_4 was coated on the CS layer at low magnifications of 0.5 μm and 500 nm, as shown in Figure 4G,H. Eg-C_3N_4/CS was clearly coated on the CS layer at 1 μm, as shown in Figure 4I, which proved the strong forces of

https://doi.org/10.1021/acsomega.1c00866
ACS Omega 2021, 6, 35221−35243

electrostatic interaction between the amine group of Eg-C_3N_4 and hydroxyl group of the CS layer. The AgNP/Eg-C_3N_4/CS nanocomposite confirmed that the AgNPs were coated on the negatively charged surface of the Eg-C_3N_4/CS composite, and it was analyzed by TEM with different magnifications of 200, 100, 100, 100, and 50 nm, as shown in Figure 4J−N. At the highest magnification of 50 nm, AgNPs were clearly coated on Eg-C_3N_4/CS, as shown Figure 4N. Further, the crystallinity of AgNPs in the AgNP/Eg-C_3N_4/CS nanocomposite was determined by selected area electron diffraction (SAED) pattern, as shown in Figure 4O. The particle size distribution in the histogram plot is shown in Figure 4O (inset). The spacing distance of the lattice border of AgNPs was clearly shown in the high-resolution TEM (HRTEM) images in Figure 4P,Q. From the TEM and HRTEM images, it was evident that AgNPs successfully self-assembled on the surface of the Eg-C_3N_4/CS composite, and this confirmed the formation of the AgNP/Eg-C_3N_4/CS nanocomposite and enhanced the catalytic activity.

2.2.12. XPS Study. X-ray photoelectron spectroscopy (XPS) was conducted to investigate the binding energy, chemical composition, and oxidation states of elements in the as-synthesized materials. The survey spectra of CS, Eg-C_3N_4/CS, and AgNP/Eg-C_3N_4/CS nanocomposites were recorded, as shown in Figure 5A(a−c). The survey spectrum of CS showed two peaks of C 1s and O 1s, as shown in Figure 5A(a). Gaussian software was used to fit the C 1s into three peaks such as C═C, C−C, and O−C═C, as shown in Figure S4A, Supporting Information. The O 1s peak was assigned to the three peaks of C═O, C−O, and O−C═C, as shown in Figure S4B, Supporting Information. These fitted curves confirmed the formation of CS by the hydrothermal method. The survey spectra of Eg-C_3N_4/CS exhibited three peaks of C 1s, N 1s, and O 1s, as shown in Figure 5A(b). Figure S5A−C, Supporting Information, shows three peaks at 284.5, 286.8, and 288.5 eV with defects of sp^2-hybridized C═C bond, sp^3-hybridized C−N bond in Eg-C_3N_4, and C═O and HO−C═O bonds in carbon spheres.[85,129] The O 1s fitting curve demonstrated two peaks at 529.5 and 532.4 eV of N−C−O and −C−O−C═O bonds due to formation of the Eg-C_3N_4/CS composite, as shown in Figure S4B, Supporting Information.[130] The N 1s fitted spectrum displayed three peaks at 396.2, 398.4, and 399.1 eV, which corresponded to tertiary nitrogen of N−$(C)_3$, triazine units of C═N−C, and the amine group of C−N−H, respectively, and were protonated with the positive charge of the −C−N bond, as shown in Figure S5C, Supporting Information.[46,131] These results showed that the self-assembled Eg-C_3N_4 on CS formed the Eg-C_3N_4/CS composite. Figure 5A(c) shows the spectrum of the AgNP/Eg-C_3N_4/CS nanocomposite in which the four peaks of C 1s, N 1s, O 1s, and Ag 3d appeared. The C 1s spectrum was centered at 282.5 eV for the C═C bond, 284.2 eV for the C−N bond in Eg-C_3N_4, and C═O and O−C═O bonds in CS, as shown in Figure 5B. The fitting curve of O 1s was splitted into three peaks at 536.5 and 537.2 eV, which corresponded to C−OH/C−O−C bonds in CS and N−C−O bonds in Eg-C_3N_4, as shown in Figure 5C. Figure 5D shows that the N 1s fitted curve had three peaks at 397.6 eV for the sp^2 C═N−C bond and 398.5 and 399.8 eV of N−$(C)_3$ bonds in Eg-C_3N_4.[132] The deconvoluted spectrum of AgNPs was splitted into four peaks at 365.2 eV, 368.4 eV (Ag $3d_{5/2}$) and 371.6 eV and 374.4 eV ($3d_{3/2}$), as shown in Figure 5E. From these binding energies, 368.4 and 374.4 eV indicated the presence of metallic silver (Ag^0) on the AgNP/Eg-C_3N_4/CS nanocomposite.[82,133]

2.3. Catalyst Testing for Conversion Cr(VI) to Cr(III). Catalytic reduction of Cr(VI) to Cr(III) ($K_2Cr_2O_7$, 20 ppm) was determined by Bg-C_3N_4, Eg-C_3N_4, CS, Eg-C_3N_4/CS, and AgNP/Eg-C_3N_4/CS nanocomposites (15 mg) as catalysts in the presence of HCOOH (2 mM, 50 mL) as a reducing agent at 45 °C at different time intervals of 0−28 min. Similar experiments were conducted without the respective catalysts. The catalytic performance for Cr(VI) to Cr(III) reduction was monitored by UV−visible spectroscopy with a peak at 350 nm.[134] Figure 6A−E shows that the catalytic reduction of Cr(VI) to Cr(III) was recorded in the presence of HCOOH without and with a catalyst at various time intervals of 0−28 min. The conversion of Cr(VI) to Cr(III) absorption peaks was not altered at 350 nm at different time intervals of 0−28 min due to high kinetic barriers between $Cr_2O_7^{2-}$ and FA without a catalyst, as shown in Figure 6A−E. The catalysts of Bg-C_3N_4, Eg-C_3N_4, CS, and Eg-C_3N_4/CS had not completely reduced Cr(VI) to Cr(III), as shown in Figure 6A−D. The yellow Cr(VI) regularly turned colorless due to the formation of Cr(III) in the presence of FA with the AgNP/Eg-C_3N_4/CS nanocomposite as the catalyst with increasing times of 0−28 min, as shown in Figure 6E. The AgNP/Eg-C_3N_4/CS nanocomposite therefore showed higher catalytic activity when compared to Bg-C_3N_4, Eg-C_3N_4, CS, and Eg-C_3N_4/CS. This AgNP/Eg-C_3N_4/CS nanocomposite's capability of reduction of Cr(VI) to Cr(III) was also confirmed with the addition of excess NaOH to produce the green precipitate of $Cr(OH)_6^{3-}$, as shown in Figure 6E, inset.

Figure 6F shows the catalytic reduction efficiency of Cr(VI) to Cr(III), which was evaluated with a plot of $\alpha = C_I - C_F/C_I \times 100$ vs time by eq 13. The catalytic detoxification of Cr(VI) to Cr(III) is illustrated in the plot of $\alpha = C_I - C_F/C_I \times 100$ vs time with different catalysts of Bg-C_3N_4, Eg-C_3N_4, CS, Eg-C_3N_4/CS, and AgNP/Eg-C_3N_4/CS nanocomposites, as shown in Figure 6F. From Figure 6F, the AgNP/Eg-C_3N_4/CS nanocomposite exhibited 98.51% conversion of Cr(VI) to Cr(III) when compared to the other catalysts of CS/Eg-C_3N_4 (33.35%), CS (5.59%), Eg-C_3N_4 (12.60%), and Bg-C_3N_4 (8.51%) because of the synergistic effect of the AgNP/Eg-C_3N_4/CS nanocomposite and $Cr_2O_7^{2-}$ in the presence of FA. Therefore, AgNPs were an effective nanocatalyst in the AgNP/Eg-C_3N_4/CS nanocomposite for the catalytic reduction of Cr(VI) to Cr(III) due to the initial adsorption of FA on the AgNP/Eg-C_3N_4/CS nanocomposite to form CO_2 and H_2 and then the catalytic conversion of Cr(VI) to Cr(III) due to intermolecular interaction, charge-transfer reaction, physisorption, and electrostatic interaction forces between Cr(VI) and the AgNP/Eg-C_3N_4/CS nanocomposite.[135,136]

The catalytic reduction rate constant of Cr(VI) to Cr(III) was computed from the plot of $\ln(C_t/C_0)$ vs time (t) with the various catalysts of Bg-C_3N_4, Eg-C_3N_4, CS, Eg-C_3N_4/CS, and AgNP/Eg-C_3N_4/CS nanocomposites, as shown in Figure 6G. The rate of reaction was dependent on the reducing action of FA and not Cr(VI) ions because of the higher concentration of FA vs Cr(VI) ions. Hence, the reaction rate constant might be pseudo-first-order kinetic, as shown in eq 1

$$\ln\left(\frac{C_t}{C_0}\right) = -Kt \tag{1}$$

where C_0 and C_t represent the intensities of the absorbance at initial time ($t = 0$) and time t, respectively. The AgNP/Eg-C_3N_4/CS nanocomposite showed a higher rate constant (k = 0.0621 min^{-1}) when compared to the other catalysts Eg-C_3N_4/CS ((k =

https://doi.org/10.1021/acsomega.1c00866
ACS Omega 2021, 6, 35221−35243

Table 1. Comparison of Catalytic Reduction of Cr(VI) into Cr(III) on the AgNP/Eg-C_3N_4/CS Nanocomposite with Other Reported Nanocomposites

catalysts	dosage	Cr(VI) concentration	TOF (min^{-1})	pH	efficiency (%)	rate constant (k) (min^{-1})	ref
Pd/GO	0.05	2.0 mM	3.6				47
Pd@GAC	2.0	0.8 mM	358.1			0.4210	48
Pd-CNTs	1.0 mol %	1.0 mM				0.31	49
Ni@C-dots	0.5 mL	1 mM					50
Ag−Au/RGO	0.5 mg	0.1 mM	186.2		99.6	2.5793×10^{-2}	51
Ni@GR-Cu	4 mg	100 mg/L	0.024	2.0		0.344	52
Pd@SiO_2−NH_2	15.00 mg/mL	6.0 mM	258	3.0	>85.0	0.094−0.363	53
PANI/MnO_2/TiO_2	1.0 mg/mL	2 mM	0.3333	2	99.90	15.97×10^{-2}	54
Pt/Pd NPs	15 mg	20 mM	1.0×10^{18}			0.133	55
palladium (Pd) tetrapods	2.0 g	2 mM				0.571	56
AgCl@Ag CS−NCs	20 mg	0.2 mM		2.0		0.125	57
Ag/SnO_2/NiO	1 g/L	20 mg/L		2.0	98	0.023	58
CdS/RGO	2.5×10^{-2} g L^{-1}	1×10^{-5} M				4.36×10^{-3}	59
PANI-sensitized g-C_3N_4/$ZnFe_2O_4$	0.2 g	20 ppm		2.0	74.0	0.0326	60
g-Fe_3O_4/RGO	1 g/L	50 ppm		2.0	97		61
mesoporous CuO/ZrO_2-MCM-41	1 g/L	20 mg/L		4.0	99		62
α-MnO_2@RGO nanorods	1 g/L	10 mg /L			97		63
G-Fe_3O_4 and Au/G-Fe_3O_4	0.02 g	10 ppm				0.0313	64
α-FeOOH nanorod/RGO	1 g/L	10 mg/L			94		65
$Gd(OH)_3$ nanorod/RGO	1 g/L	10 mg/L			83		66
p−n heterojunction of $MCeO_2$−$BiFeO_3$	20 mg	10 ppm			98.2	0.06533	67
Bi/Bi_2MoO_6	0.02 g	100 mg/L		2	97	0.014	68
Ag@Ag_3PO_4/g-C_3N_4/NiFe layered double hydroxide	0.02 g	20 ppm		5	97	0.0041	69
AgNP/Eg-C_3N_4/CS nanocomposite	15 mg	20 ppm	0.01587	2.0	98.5	6.21×10^{-2}	this work

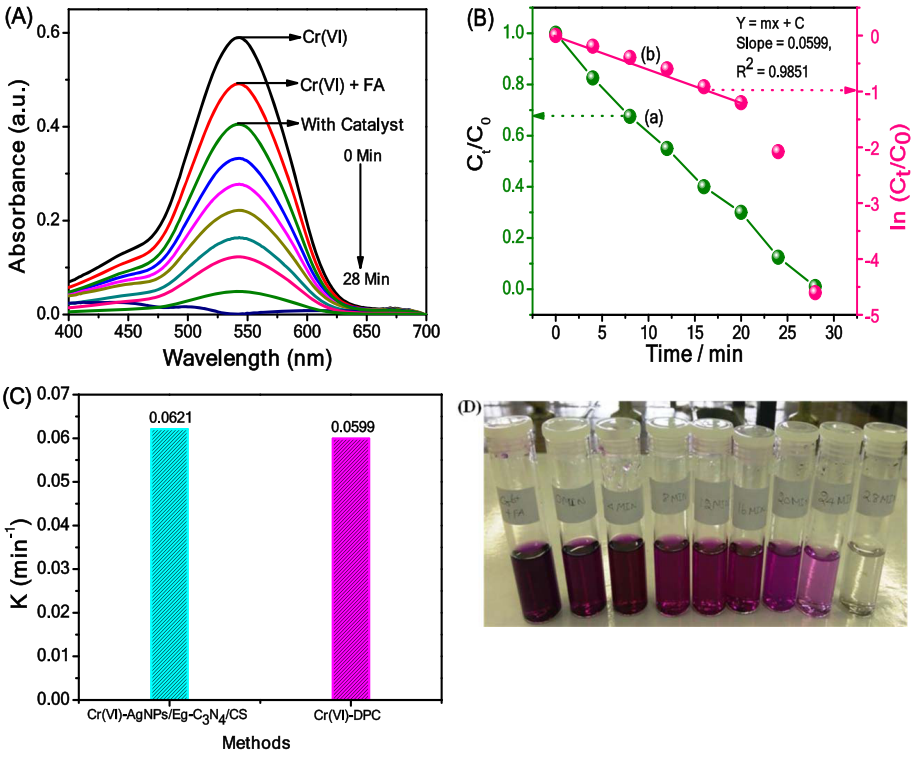

Figure 7. (A) UV−visible spectra of catalytic reduction of Cr(VI)-DPC with the AgNP/Eg-C_3N_4/CS nanocomposite, (B) calibration plot of (C_t/C_0) and ln(C_t/C_0) vs time for reduction of Cr(VI) with the AgNP/Eg-C_3N_4/CS nanocomposite, (C) comparison plot of kinetic rate constant vs methods, and (D) digital image of successive reduction of Cr(VI) by the Cr(VI)-DPC method.

0.0146 min^{-1}), Eg-C_3N_4 (k = 0.0019 min^{-1}), Bg-C_3N_4 (k = 0.0036 min^{-1}), and CS (k = 0.0021 min^{-1}), as shown in Figure 6G. It was observed that the AgNP/Eg-C_3N_4/CS nanocomposite showed better catalytic conversion of Cr(VI) to Cr(III) in the presence of FA. The catalytic activity of the AgNP/Eg-C_3N_4/CS nanocomposite was compared with other

https://doi.org/10.1021/acsomega.1c00866
ACS Omega 2021, 6, 35221−35243

nanocomposites, as mentioned in Table 1. Furthermore, the turnover frequency (TOF) was evaluated for the catalytic activity of Bg-C_3N_4, Eg-C_3N_4, CS, Eg-C_3N_4/CS, and AgNP/Eg-C_3N_4/CS nanocomposites by eq 2. The AgNP/Eg-C_3N_4/CS nanocomposite showed a higher TOF value of 0.01587 min^{-1}, as shown in Table 1. Among them, the AgNP/Eg-C_3N_4/CS nanocomposite recorded excellent catalytic activity when compared to the other catalyst materials.

2.3.1. Comparison Study with the 1,5-Diphenylcarbazide (DPC) Method. Further, the catalytic activity of the AgNP/Eg-C_3N_4/CS nanocomposite was also investigated for the reduction of Cr(VI) by measuring the accurate concentration between the absorption peak of DPC−Cr(VI) at 540 nm and simulated formic acid at various time intervals. During the catalytic reduction method, the absorption spectra at 540 nm was regularly reduced due to the concentration of Cr(VI)-DPC decreasing gradually, and it was completely decolorized after 28 min, which demonstrates that the catalytic reduction of Cr(VI) to Cr(III) using the AgNP/Eg-C_3N_4/CS nanocomposite has occurred, as shown in Figure 7A. In the meantime, the Cr(VI) concentration was reduced with different time intervals from 0 to 28 min.

The catalytic activity of the AgNP/Eg-C_3N_4/CS nanocomposite at various time intervals and concentrations of Cr(VI) is determined by a plot of C_t/C_0 vs time, as shown in Figure 7B(a). According to eq 1, the pseudo-first-order reaction kinetic rate constant of the AgNP/Eg-C_3N_4/CS nanocomposite is k = 0.0599 min^{-1}, as shown in Figure 7B(b). The k value (0.0599 min^{-1}) for the Cr(VI)-DPC method was slightly below the value obtained for the Cr(VI)-AgNP/Eg-C_3N_4/CS nanocomposite method (k = 0.0621 min^{-1}), as shown in Figure 7C. Figure 7D shows the digital image of the catalytic reduction of Cr(VI) by the Cr(VI)-DPC method with a color change from violet to colorless. Therefore, the AgNP/Eg-C_3N_4/CS nanocomposite was suitable for the catalytic reduction Cr(VI) to Cr(III).[57,137]

2.3.2. Effect of Catalyst Dosage. The optimized catalyst dosage was very important to identify the catalytic reduction of Cr(VI) to Cr(III) by changing the catalyst dosage of 5, 10, and 15 mg of AgNP/Eg-C_3N_4/CS nanocomposite in the presence of FA at 0−28 min, as shown in Figure S6A−C, Supporting Information. The results showed that the catalytic reduction percentages of 45.6, 76.8, and 98.5% corresponded to different catalyst weights of 5, 10, and 15 mg of AgNP/Eg-C_3N_4/CS nanocomposite, respectively as shown in Figure S6D, Supporting Information. The kinetic rate constant was obtained from the plot of $\ln(C_t/C_0)$ vs time, k = 0.0184, 0.452, and 0.0620 min^{-1}, which corresponded to 5, 10, and 15 mg of AgNP/Eg-C_3N_4/CS nanocomposite, as shown in Figure S6E, Supporting Information. The results confirmed that 15 mg of AgNP/Eg-C_3N_4/CS nanocomposite diminished the yellow Cr(VI) to colorless Cr(III) within 0−28 min with FA. This higher catalyst dosage of AgNP/Eg-C_3N_4/CS nanocomposite resulted in the rapid reduction of Cr(VI) to Cr(III) within 0−28 min due to increased active sites and a better reducing agent like FA to produce H_2 and CO_2.[138] Further, the kinetic studies were performed for the conversion of Cr(VI) to Cr(III) with 15 mg of AgNP/Eg-C_3N_4/CS nanocomposite as the catalyst.

2.3.3. Effect of Concentration. Different Cr(VI) concentrations (5, 10, 15, and 20 ppm) were used with AgNP/Eg-C_3N_4/CS nanocomposite and FA, as shown in Figure S7A−D, Supporting Information. The catalytic reduction of Cr(VI) to Cr(III) was rapid (within 0−8 min) for the lower concentration of Cr(VI) (5 ppm) and higher catalytic activity sites of 15 mg of AgNP/Eg-C_3N_4/CS nanocomposite, as shown in Figure S7A, Supporting Information. The Cr(VI) concentration was increased to about 10 and 15 ppm and the catalytic reduction time was also increased 0−12 and 0−18 min, respectively, under the same conditions, as shown in Figure S6B,C, Supporting Information. The higher concentration of 20 ppm of Cr(VI) uniformly decreased the peak intensity and also decolorized Cr(VI) with the AgNP/Eg-C_3N_4/CS nanocomposite at 0−28 min, as shown in Figure S7D, Supporting Information. Concentrations above 20 ppm reduced the catalytic reduction of Cr(VI) to Cr(III) under the same conditions because of higher quantities of Cr(VI) ions that block the active sites and enhance the shielding effect of the AgNP/Eg-C_3N_4/CS nanocomposite, as a result of minimized decomposition of FA and less conversion of Cr(VI) to Cr(III).[139] From the results, 20 ppm of Cr(VI) was suitable for the catalytic study.

Figure S6E,F (Supporting Information) shows the percentage of catalytic reduction and kinetic rate constants of Cr(VI) to Cr(III) reductions with various concentrations of 5, 10, 15, and 20 ppm. The highest percentage conversion of Cr(VI) to Cr(III) was at 20 ppm (98.5%) when compared to 15 ppm (96.90%), 10 ppm (97.16%), and 5 ppm (96.5%), as shown in Figure S7E, Supporting Information. The rate constants of Cr(VI) to Cr(III) reduction were k = 0.0620, 0.163, 0.285, and 0.4023 min^{-1} with corresponding concentrations of 20, 15, 10, and 5 ppm, respectively, as shown in Figure S7F, Supporting Information. The data confirmed that the optimized concentration of Cr(VI) was 20 ppm.

2.3.4. Effect of Temperature. The effect of temperature (25, 35, and 45 °C) was studied for the catalytic reduction of Cr(VI) to Cr(III) with 15 mg of AgNP/Eg-C_3N_4/CS nanocomposite in the presence of FA at 0−28 min, as shown in Figure S8A−C, Supporting Information. Figure S8A shows that the catalytic reduction of Cr(VI) did not show complete decolorization at 25 °C with different time intervals of 0−28 min. The conversion of Cr(VI) to Cr(III) was partially conducted at 35 °C with 0−28 min, as shown in Figure S8B, Supporting Information. At a higher temperature of 45 °C, the catalytic reduction of Cr(VI) to Cr(III) gradually reduced the peak intensity at 350 nm and 0−28 min, as shown in Figure S8C, Supporting Information. The catalytic conversion of Cr(VI) to Cr(III) was well performed at a higher temperature of 45 °C with the AgNP/Eg-C_3N_4/CS nanocomposite at 0−28 min due to better decomposition of FA to CO_2 and H_2 followed by the reduction of Cr(VI).[140] The reduction percentage of Cr(VI) to Cr(III) is as follows: 45 °C (90.0%), 35 °C (44.54%), and 25 °C (39.67%), as shown in Figure S8D, Supporting Information. The kinetic rate constant k values were derived from the plot ln (C_t/C_0) vs time, as shown in Figure S8E, Supporting Information. Higher conversion percentage (90.0%) and kinetic rate constant (0.0762 min^{-1}) were evaluated at a higher temperature of 45 °C due to heat energy required for the catalytic reduction of Cr(VI) to Cr(III).[141−144]

2.3.5. Effect of pH. The effective catalytic reduction of Cr(VI) to Cr(III) was dependent on the pH of different solutions because of the surface charge of the catalyst and different species of chromium(VI) at pH 2.0 ($H_2Cr_2O_7$), pH 2.0−6.0 ($Cr_2O_7^{2-}$ and $HCrO_4^-$), and pH 6.8 (CrO_4^{2-}) in solution.[145,146] The pH of solutions of Cr(VI) (20 ppm) was varied at 2, 4, and 6, and the catalytic activity for the detoxification of Cr(VI) was evaluated with 15 mg of AgNP/Eg-C_3N_4/CS nanocomposite in the presence of FA at 0−28 min, as shown in Figure S9A−C,

https://doi.org/10.1021/acsomega.1c00866
ACS Omega 2021, 6, 35221−35243

Supporting Information. Figure S9A shows that pH 2.0 exhibited the highest catalytic reduction of Cr(VI) to Cr(III) because Cr(VI) dissociates into various types of ions such as $HCrO_4^-$ and $Cr_2O_7^{2-}$ at lower pH.[147] The maximum absorption peak of Cr(VI) at 350 nm was observed under acidic conditions (pH 2) because of the protonation of CrO_4^{2-} to form $HCrO_4^-$, and this result is consistent with that reported in the literature.[148] Figure S9B,C shows that at pH 4 and 6 incomplete reduction of Cr(VI) to Cr(III) occurred due to electrostatic repulsion between the negative charge of the catalyst of AgNP/Eg-C_3N_4/CS nanocomposite and negative charge of Cr(VI).[149] At high pH 4−6, the major species is CrO_4^{2-} in solution and the Cr(VI) solution color changed from light yellow to intense yellow, which corresponded to a shift in the absorption peak position with pH.[150] This effect was also observed in a previous report.[151] The percentage reduction of Cr(VI) to Cr(III) was calculated at pH 2 (80.3%), pH 4 (69.7%), and pH 6 (59.4%), as shown in Figure S9D, Supporting Information. In highly acidic solutions, Cr(VI) to Cr(III) displayed higher reduction efficiency (80.3%) and rate constant (0.0488 min^{-1}) due to the positive charge of the AgNP/Eg-C_3N_4/CS nanocomposite and negative charge of $HCrO_4^-$ and $Cr_2O_7^{2-}$, as shown in Figure S9E, Supporting Information.[152] Under basic conditions, the rate constant decreased because of the precipitation of CrO_4^{2-} to $Cr(OH)_3$, and it created a negative charge on the AgNP/Eg-C_3N_4/CS nanocomposite. Hence, the catalytic reduction of Cr(VI) to Cr(III) was favored at acidic pH 2 with the AgNP/Eg-C_3N_4/CS nanocomposite than at pH 4 and 6.[28] The catalytic reduction of Cr(VI) to Cr(III) is shown with acid, neutral, and base conditions in eqs 2−4.[153,154]

Acidic condition

$$Cr_2O_7^{2-} + 14H^+ + 6e^- \rightarrow 2Cr^{3+} + 7H_2O \quad (2)$$

Neutral condition

$$CrO_4^{2-} + 8H^+ + 3e^- \rightarrow 2Cr^{3+} + 7H_2O \quad (3)$$

Basic condition

$$CrO_4^{2-} + 4H_2O + 3e^- \rightarrow Cr(OH)_3 + 5OH^- \quad (4)$$

2.3.6. Interference and Stability Studies. The interference study was investigated using different inorganic (NaCl, NaF, KCl, and K_2HPO_4) and organic (starch, D-dextrose, cellulose, urea, and citric acid) compounds with the AgNP/Eg-C_3N_4/CS nanocomposite under the same conditions. This showed promising performance of the AgNP/Eg-C_3N_4/CS nanocomposite for catalytic reduction of Cr(VI) to Cr(III) with FA in the presence of inorganic and organic compounds in wastewater. Figure 8A shows the plot of reduction efficiency (%) vs various interferences was slightly changed in the conversion of Cr(VI) to Cr(III) with AgNP/Eg-C_3N_4/CS nanocomposite because of low interaction of inorganic and organic substances during the reduction of Cr(VI). The stability test is very important for the reuse and efficiency of the AgNP/Eg-C_3N_4/CS nanocomposite after reduction of Cr(VI) to Cr(III). The nanocomposite was washed with distilled water in every process and dried at room temperature, and it was applied into a newly prepared Cr(VI) solution. The AgNP/Eg-C_3N_4/CS nanocomposite did not reduce the catalytic activity much after six cycles, as shown in Figure 8B. Further, it maintained the same morphology as shown by TEM and FT-IR after reuse for the reduction of Cr(VI) to Cr(III), as shown in Figure 9A−C. The

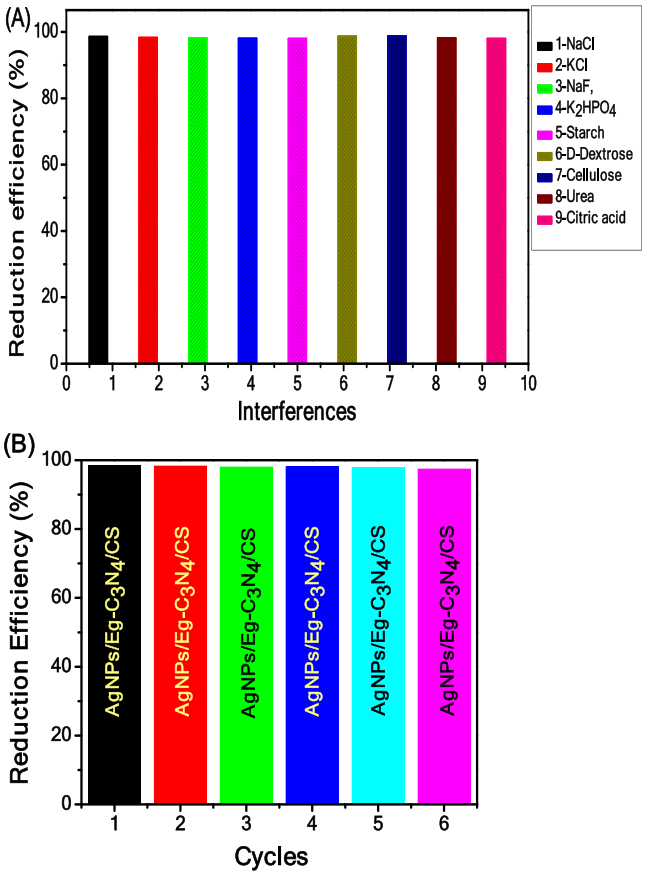

Figure 8. (A) Plot of catalytic conversion % vs interference study of catalytic reduction Cr(VI) to Cr(III) after addition of (1) NaCl, (2) KCl, (3) NaF, (4) K_2HPO_4, (5) starch, (6) D-dextrose, (7) cellulose, (8) urea, and (9) citric acid with the AgNP/Eg-C_3N_4/CS nanocomposite and (B) stability of the AgNP/Eg-C_3N_4/CS nanocomposite for catalytic reduction of Cr(VI) to Cr(III) in FA after six repeated recycles.

above test confirmed that the AgNP/Eg-C_3N_4/CS nancomposite was a better catalyst with good stability.

To study the catalytic reduction mechanism of the reduction of Cr(VI) to Cr(III), a H_2 generation experiment was conducted. According to the reaction pathway of $Cr_2O_7^{2-} + 14H^+ + 6e^- \rightarrow 2Cr^{3+} + 7H_2O$,[155] the catalytic reduction of Cr(VI) to Cr(III) was illustrated by FA ($HCOOH \rightarrow CO_2 + H_2$) as a strong reducing agent and generated H_2 on the metal catalyst surface.[156−158] The suitable decomposition of the FA reaction was conducted on the surface of the AgNP/Eg-C_3N_4/CS nanocomposite.[159] FA was initially adsorbed on the AgNP/Eg-C_3N_4/CS nanocomposite surface followed by decomposition to CO_2 and H_2.[160] Then, electrons were transferred from Cr(VI) to Cr(III) on the surface of the AgNP/Eg-C_3N_4/CS nanocomposite under the H_2 reaction pathway. Similar results have been reported for the reduction of Cr(VI) to Cr(III) on Pd_3Ag_1/GO−NH_2 and Pd-on-Au bimetallic catalysts.[25,161] Finally, Cr(III) was adsorbed from the AgNPs on the Eg-C_3N_4/CS surface. Reduced Cr(III) was confirmed by an excess amount of NaOH to obtain a green color of $[Cr(OH)_6]^{3-}$.[162] Further, Cr(III) was also evident using H_2O_2 as a oxidizing agent to produce a yellow solution of Cr(VI) ions. The catalytic reduction mechanism of Cr(VI) to Cr(III) is displayed in Scheme 1.

https://doi.org/10.1021/acsomega.1c00866
ACS Omega 2021, 6, 35221−35243

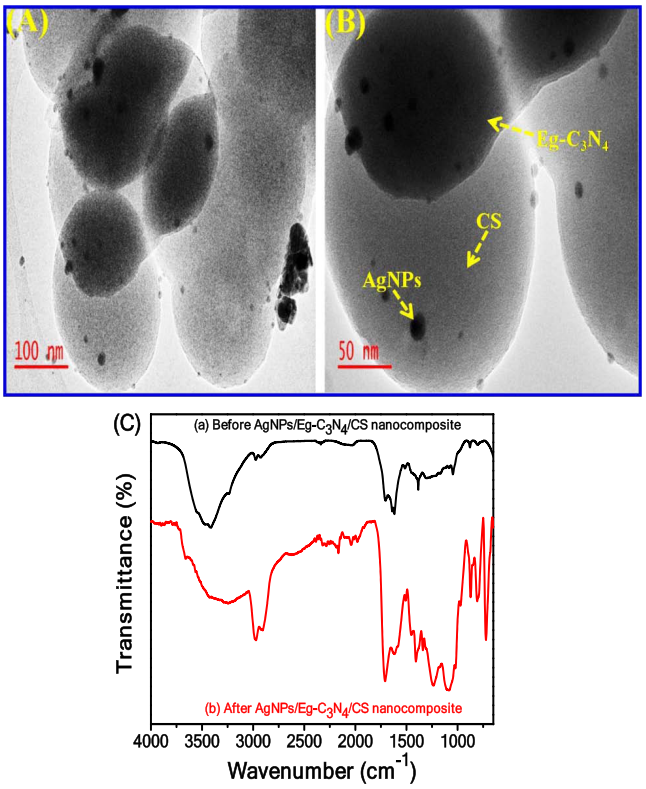

Figure 9. (A–C) TEM images of the AgNP/Eg-C_3N_4/CS nanocomposite after six recycles at (A) 100 nm and (B) 50 nm and (C) FT-IR spectra of the AgNP/Eg-C_3N_4/CS nanocomposite before and after reduction of Cr(VI) to Cr(III).

2.3.7. Reusability Evaluation of Photocatalytic Activity. The reuse of the Cr(III)-AgNP/Eg-C_3N_4/CS nanocomposite (100 mg) was analyzed for the photocatalytic degradation of MB (1 mM in 100 mL of H_2O) under visible light irradiation with various time intervals and also compared with that of the AgNP/Eg-C_3N_4/CS nanocomposite. The photocatalytic degradation of MB was conducted with the AgNP/Eg-C_3N_4/CS nanocomposite and Cr(III)-AgNP/Eg-C_3N_4/CS nanocomposite under visible light irradiation at different time intervals, as shown in Figure 10A,B. First, MB was adsorbed before and after reduction of Cr(VI) nanocomposites under dark conditions at 30 min and irradiated with visible light at different time intervals. Figure 10A shows that the photocatalytic degradation of MB was achieved with the AgNP/Eg-C_3N_4/CS nanocomposite under visible light irradiation at 0–90 min but the Cr(III)-AgNP/Eg-C_3N_4/CS nanocomposite speedily degraded MB under visible light irradiation within 0–70 min, as shown in Figure 10B. In total, 97.95% degradation of MB was obtained using the Cr(III)-AgNP/Eg-C_3N_4/CS nanocomposite as compared to that using the AgNP/Eg-C_3N_4/CS nanocomposite (94.89%) due to the large surface area after doping with Cr(III) thereby resulting in lower electron–hole recombination rate, as shown in Figure 10C. The degradation rate constants of the AgNP/Eg-C_3N_4/CS nanocomposite (k = 0.0306 min^{-1}) and Cr(III)-AgNP/Eg-C_3N_4/CS nanocomposite (k = 0.0589 min^{-1}) were calculated by the pseudo-first-order kinetic equation (eq 2), and these were obtained from the plot of $\ln(C_t/C_0)$ vs times, as shown in Figure 10D. From these results, the Cr(III)-AgNP/Eg-C_3N_4/CS nanocomposite promised great photocatalytic activity and better reusability than the AgNP/Eg-C_3N_4/CS nanocomposite. This Cr(III)-AgNP/Eg-C_3N_4/CS nanocomposite was also compared with other nanocomposites for MB photocatalytic degradation efficiency, as shown in Table S1, Supporting Information.[163−168] In addition, there was almost little to no conversion of Cr(III) to Cr(VI) observed after the photocatalytic degradation process. The Cr(VI) concentration is negligible and will be difficult to be determined in solution. Thus, reuse in the photocatalytic degradation process does not result in any further or undesirable environmental hazards.[169] Moreover, the Eg-C_3N_4 and CS components of the Cr(III)-AgNP/Eg-C_3N_4/CS nanocomposite are supported to absorb Cr(III) into their active sites from the solution, which enables the Cr(III)-AgNP/Eg-C_3N_4/CS nanocomposite to enhance the photocatalytic degradation activity during the reaction.

2.3.8. Photocatalytic Degradation Mechanism of MB with the Cr(III)-AgNP/Eg-C_3N_4/CS Nanocomposite. Based on the data and discussion above, the photocatalytic degradation mechanism of MB on the Cr(III)-AgNP/Eg-C_3N_4/CS nanocomposite is described, as shown in Scheme 2. When the visible light was irradiated on CS (3.54 eV), the electrons were excited from the valence band (VB) to the conduction band (CB), and this transferred the conduction band electrons to Eg-C_3N_4 due to lower band gap energy (2.7 eV).[170] Additionally, the conduction band (CB) electrons in Eg-C_3N_4 were immediately transferred to AgNPs because of the lower band gap energy of Eg-C_3N_4 compared to that of CS and then the accumulated electrons rapidly moved to the metallic AgNPs that act as electron-scavenging centers.[171,172] Again, the same CB electrons of AgNPs moved to Cr(III) present at the interface of CS because of a reduction in the electron–hole pair recombination rate. The electrons in the CB of Cr(III) have a strong reduction power, whereas the holes in the VB of Ag display a strong oxidation ability. The high reducing electrons located on the CB of Cr(III) would react with O_2 to form $O_2^{\bullet-}$.[173] This can further oxidize MB. The holes located on the VB of Ag would photocatalytically oxidize H_2O, giving rise to an $^{\bullet}OH$ radical, which in turn will oxidize MB.[174,175] Simultaneously, parts of photoinduced electrons on the CB of CS are involved in the reduction of O_2 to yield $O_2^{\bullet-}$ due to more negativity.[176] These superoxide radical anions and hydroxyl radicals were highly oxidant to degrade the MB dyes, as shown in Scheme 2. The Cr(III)-AgNP/Eg-C_3N_4/CS nanocomposite efficiently exhibited the photocatalytic activity for MB degradation and also displayed reusability. The various possible reaction steps involved in the photocatalytic degradation of dyes are illustrated through the following equations (eqs 5–12)

$$CS + h\nu \rightarrow CS(h^+(VB)) + CS(e^-(CB)) \quad (5)$$

$$CS(e^-(CB)) + Eg - C_3N_4 \rightarrow CS + Eg - C_3N_4(e^-) \quad (6)$$

$$Eg - C_3N_4(e^-) + AgNPs \rightarrow Eg - C_3N_4 + AgNPs(e^-) \quad (7)$$

$$AgNPs(e^-) + Cr(III) \rightarrow Cr(III)(e^-) + AgNPs \quad (8)$$

$$Cr(III)(e^-) + O_2 \rightarrow O_2^{\bullet-} \quad (9)$$

$$AgNPs(h^+(VB)) + OH/H_2O \rightarrow AgNPs + {}^{\bullet}OH \quad (10)$$

$$^{\bullet}OH + MB \rightarrow CO_2 + H_2O \quad (11)$$

$$O_2^{\bullet-} + MB \rightarrow CO_2 + H_2O \quad (12)$$

https://doi.org/10.1021/acsomega.1c00866
ACS Omega 2021, 6, 35221−35243

Scheme 1. Catalytic Reduction of Cr(VI) to Cr(III) with the AgNP/Eg-C_3N_4/CS Nanocomposite Using FA and Digital Images of Reduction of Cr(VI) to Cr(III) Colorless Solution and Green Color Solution of $[Cr(OH)_6]^{3-}$ and Excessive Addition of NaOH Solution for Confirmation of Cr(III) Reduction[1]

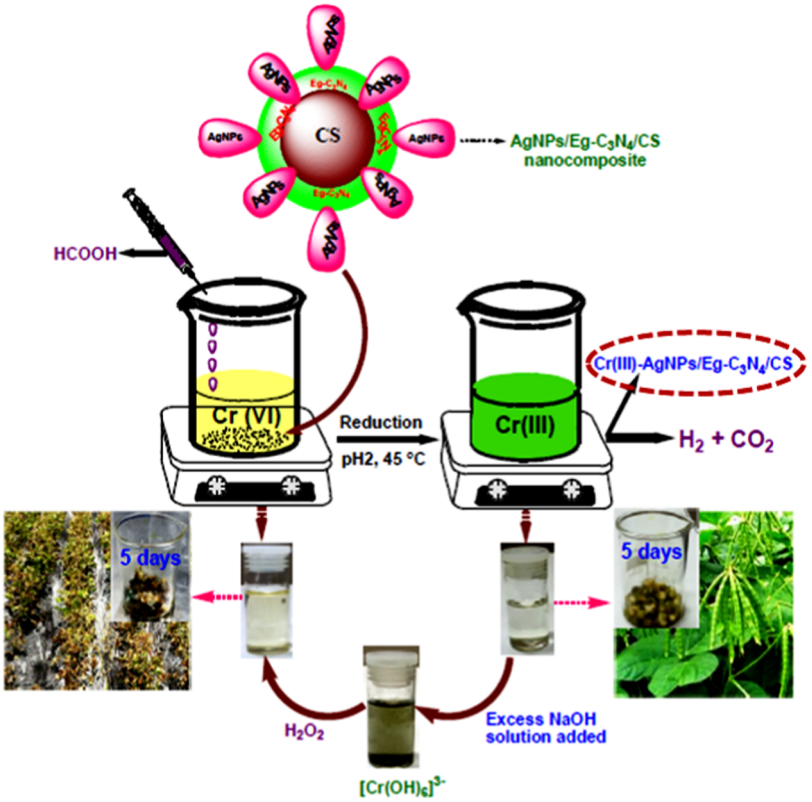

[1]Cytotoxicity study of before (left) and after (right) reduction of Cr(VI) with mung bean germination images after 5 days.

Furthermore, the Cr(III)-AgNP/Eg-C_3N_4/CS nanocomposite photocatalyst was compared with other literature-reported nanocomposites. This reusable nanocomposite has improved the photocatalytic degradation of MB when compared to the results in previously reported works.

A reactive species investigation was conducted to determine the role of the reactive species created during the photocatalytic degradation of methylene blue with Cr(III)-AgNP/Eg-C_3N_4/CS under visible light irradiation at various time intervals of 0−90 min. The superoxide radicals ($^{\bullet}O^{2-}$), hydroxide radicals ($^{\bullet}OH$), and holes (h^+) were generated, and these corresponded to isopropyl alcohol (IPA), *p*-benzoquinone (BQ), and ethylenediaminetetraacetic acid (EDTA) as the scavengers, respectively.[177] The degradation efficiency of MB was 97.95% in the absence of scavengers after 90 min. IPA, BQ, and EDTA scavengers were added to the reaction mixture, and the degradation efficiency of MB was 96.82, 90.76, and 65.25%, respectively, as shown in Figure 11A. From the results, the superoxide radicals (IPA) reactive species was effectively involved in the photocatalytic degradation of MB when compared to the other systems of BQ and EDTA.[178,179] Hence, the photocatalytic degradation of MB was significantly reduced due to the addition of IPA to photogenerated hydroxide radicals ($^{\bullet}OH$) and the degradation efficiency was slightly varied after the addition of BQ and EDTA scavengers.[180]

Further, the potential of conduction band (E_{CB}) and potential of valence band (E_{VB}) of CS, Eg-C_3N_4, AgNPs, and Cr were also calculated from the following equations[181]

$$E_{VB} = \chi - E_e + 1/2E_g \quad (13)$$

$$E_{CB} = E_{VB} - E_g \quad (14)$$

where χ is the electronegativity of CS (2.5 eV), Eg-C_3N_4 (4.72 eV), Ag (1.93 eV), and Cr (1.7 eV); E_e is the energy of free electrons on the hydrogen scale (about 4.5 eV); and E_g is the band gap energy of CS (3.42 eV), Eg-C_3N_4 (2.7 eV), AgNPs (2.73 eV), and Cr (3.2 eV). By the calculation, E_{VB} and E_{CB} potentials of CS were found to be 2.79 and −0.63 eV, respectively. E_{VB} and E_{CB} potentials of Eg-C_3N_4 were found to be 2.52 and −0.18 eV, respectively. E_{VB} and E_{CB} potentials of AgNPs were found to be 1.98 and −0.75 eV, respectively, and E_{VB} and E_{CB} potentials of Cr(III) were found to be 2.63 and −0.59 eV, respectively.

Holes in E_{VB} of AgNPs could move to Eg-C_3N_4, where electrons were often transferred from Eg-C_3N_4 (E_{CB}) to AgNPs (E_{CB}) simultaneously. These electrons and holes were effectively separated to enhance the photocatalytic activity. Even though the electrons in E_{CB} of AgNPs were transferred to O_2 to make superoxides ($^{\bullet}O^{2-}$) due to the higher positivity of AgNPs (0.75 eV vs normal hydrogen electrode (NHE)) than $O_2/^{\bullet}O^{2-}$ (−0.33 eV vs NHE),[182] this process was against the prior-reported formation of the $^{\bullet}O^{2-}$ radicals and had an important effect on the photocatalytic reaction process. Therefore, an additional method would more properly reproduce the actual mechanism. The photogenerated electrons in the E_{CB} of AgNPs were suddenly moved to the E_{CB} of Cr and followed by recombination with h^+. The highly negative position in the E_{CB} of Cr than the $O_2/^{\bullet}O^{2-}$ potential (−0.33 eV vs NHE) produced the $^{\bullet}O^{2-}$ radicals, which can directly lead to the degradation of MB to nontoxic products. Meanwhile, holes accumulated on the

https://doi.org/10.1021/acsomega.1c00866
ACS Omega 2021, 6, 35221−35243

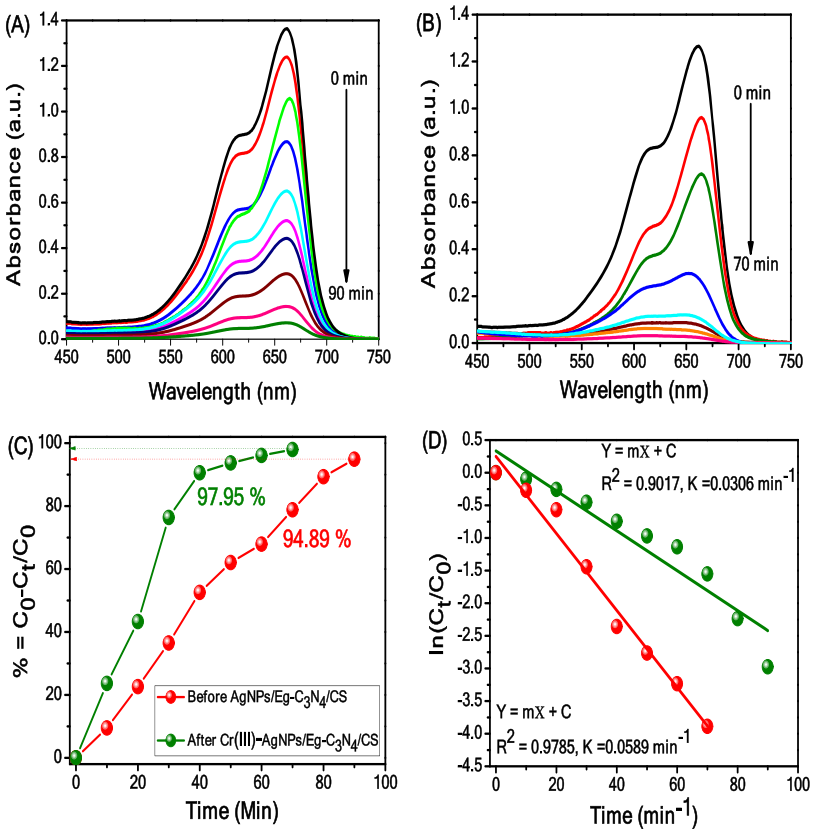

Figure 10. UV−vis spectra of (A) before AgNP/Eg-C_3N_4/CS nanocomposite and (B) after Cr(III)-AgNP/Eg-C_3N_4/CS nanocomposite the photocatalytic degradation of MB under visible light irradiation at different time intervals, (C) calibration plot of the percentage of degradation efficiency vs time before and after, and (D) plot of $\ln(C_t/C_0)$ vs time before and after.

Scheme 2. Photocatalytic Degradation Mechanism of MB by the Reusable Cr(III)-AgNP/Eg-C_3N_4/CS Nanocomposite under Visible Light Irradiation

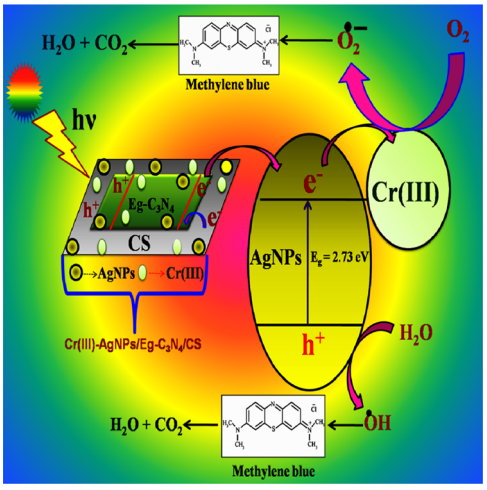

VB of AgNPs also enable direct oxidization of MB rather than oxidizing H_2O to create $^{\bullet}OH$ because the E_{VB} positions of both AgNPs and Eg-C_3N_4 were less positive than the $H_2O/^{\bullet}OH$ potential (2.73 eV vs NHE). Furthermore, the holes in VB of AgNPs (1.98 eV vs NHE) have shown a more positive potential than the redox potential of E_0 ($OH^-/^{\bullet}OH$) = 1.9 eV vs NHE).[183,184] Based on the above analysis, it indicated that ^-OH can be oxidized by holes. As such, the accumulated holes left in the VB of AgNPs will directly oxidize MB to degraded products and lead to the oxidation of H_2O to create $^{\bullet}OH$ reactive species, which consequently oxidize MB to CO_2 and H_2O.[130] The IPA scavenger was mostly involved in the degradation of MB when compared to other BQ and EDTA scavengers, as shown in Figure 11B. In general, the typical Cr(III)-AgNP/Eg-C_3N_4/CS system was suitable to enhance the photocatalytic degradation mechanism of MB. It was noted that the Cr(III)-AgNP/Eg-C_3N_4/CS nanocomposite system maintained a high potential band to improve the photocatalytic degradation performance.

2.3.9. Cytotoxicity Study In Vivo. The cytotoxicity was tested with mung green bean sprouts to determine the toxicity before and after reduction of Cr(VI) and Cr(III) solutions, respectively, in vivo after 10 days of culturing. The Cr(VI) (20 mL) and Cr(III) (20 mL) solutions were individually taken in 100 mL beakers and the mung green bean sprouts were added, as shown in Figure S10A,B, Supporting Information. The mung bean sprouts were completely damaged in the Cr(VI) solution after 5 days due to high toxicity, as shown in Figure S10A, Supporting Information. Figure S10B shows that the roots and stems were germinated in the Cr(VI) solution after 5 days. The maximum roots and stems of mung green bean were significantly germinated in Cr(III) solution because of less toxicity and also confirmed that the AgNP/Eg-C_3N_4/CS nanocomposite effectively reduced Cr(VI) to Cr(III) at pH 2.

3. CONCLUSIONS

A self-assembled AgNP/Eg-C_3N_4/CS nanocomposite was prepared by an adsorption method under room temperature. This showed good optical properties, high surface area, and large pore size. This development of the AgNP/Eg-C_3N_4/CS

https://doi.org/10.1021/acsomega.1c00866
ACS Omega 2021, 6, 35221−35243

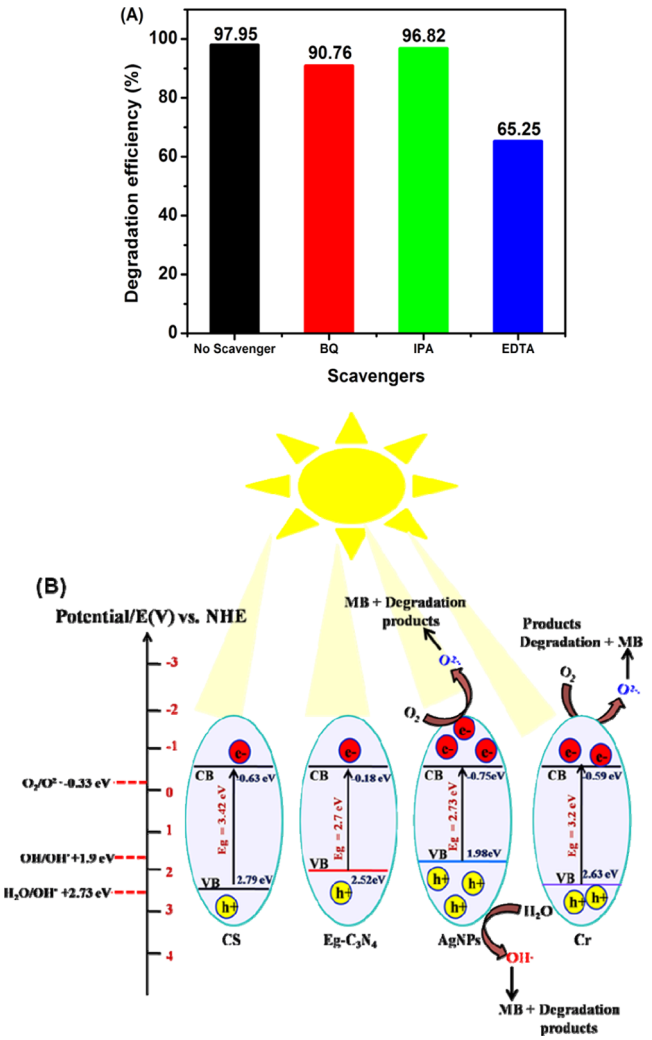

Figure 11. (A) Determination of radical scavengers for the photodegradation of MB on the Cr(III)-AgNP/Eg-C_3N_4/CS nanocomposite and (B) band structure and reaction mechanism of MB photodegradation on the Cr(III)-AgNP/Eg-C_3N_4/CS nanocomposite under visible light irradiation.

nanocomposite with AgNPs can result in improved catalytic activity due to surface plasmon resonance. Minimized photoluminescence intensity and electrochemical impedance plots with small arcs provided evidence for better charge separation and improved catalytic performance of the AgNP/Eg-C_3N_4/CS nanocomposite. The catalytic reduction activity of the AgNP/Eg-C_3N_4 nanocomposite for conversion of Cr(VI) to Cr(III) (98.5%) was significantly higher than those of Bg-C_3N_4 (8.51%), CS/Eg-C_3N_4 (33.35%), Eg-C_3N_4 (12.60%), and CS (5.59%). The AgNP/Eg-C_3N_4/CS nanocomposite was used for the catalytic reduction of Cr(VI) to Cr(III) with formic acid as a reducing agent at 45 °C and showed higher kinetic rate constant (0.0621 min^{-1}). Effects of different catalyst dosages, concentrations of Cr(VI), pH levels, and various temperatures on the catalytic reduction of Cr(VI) to Cr(III) were also studied. Under all conditions, the AgNP/Eg-C_3N_4/CS nanocomposite showed higher catalytic activity than Bg-C_3N_4, Eg-C_3N_4, CS, and Eg-C_3N_4/CS for the reduction of Cr(VI) in aqueous solutions. Moreover, it was also investigated in selectivity and stability studies with various interferences and repeated for six cycles (96.5%), respectively. The eco-friendly and economic nature of the AgNP/Eg-C_3N_4/CS nanocomposite will enable it to be prepared in large quantities for the reduction of toxic metals into nontoxic forms and can serve as a catalyst with industrial applications and good reusability and a photocatalyst as well.

4. EXPERIMENTAL SECTION

4.1. Chemicals and Reagents. Melamine, $K_2Cr_2O_7$, HCOOH, $AgNO_3$, H_2SO_4, and D-dextrose were purchased from Sigma-Aldrich. HCl, NaOH, urea, NaCl, KCl, D-dextrose, sucrose, cellulose acetate, methylene blue, Na_2SO_4, K_2HPO_4, and ethanol were brought from Merck, South Africa. Milli-Q water was used for all experiments.

4.2. Synthesis of Eg-C_3N_4 by Thermal Polycondensation. Thermal polycondensation was used to prepare Bg-C_3N_4 with melamine as precursors. Melamine (6.0 g) was crushed for 5 min and transferred in a closed ceramic crucible at 550 °C for 2 h at a heating rate of 5 °C/min in a muffle furnace. Bulk g-C_3N_4 was obtained as a yellow compound after 2 h.[185] Eg-C_3N_4 was prepared by 3.0 g of Bg-C_3N_4 and 5 M H_2SO_4 in 100 mL of water in a 250 mL beaker with sonication for 5 h. A yellow soultion formed, and it was centrifuged with water until pH 7. The precipitate was kept in a hot air oven at 60 °C for 12 h for drying. The light yellow powder confirmed the formation of protonated Eg-C_3N_4, and the formation mechanism is shown in Scheme 3.

4.3. Preparation of CS by Hydrothermal Method. The carbon spheres (CSs) were prepared by a hydrothermal method, where 6.0 g of D-dextrose in 70 mL of water was stirred for 30 min at room temperature. It was poured into a Teflon-lined autoclave at 180 °C for 10 h. The blackish-brown precipitate was centrifuged with water several times and dried at 60 °C for 12 h to get a black-brownish solid as carbon spheres (CSs).[91]

4.4. Preparation of the Eg-C_3N_4/CS Composite by Self-Assembly. The Eg-C_3N_4/CS composite was prepared by a self-assembly process. Eg-C_3N_4 (1.0 g) and 2.0 g of CS were added to 50 mL of distilled water while stirring for 12 h at room temperature. It was collected after centrifugation with water and ethanol and dried at 60 °C for 12 h.

4.5. Preparation of the AgNP/Eg-C_3N_4/CS Nanocomposite by Self-Assembly. The AgNP/Eg-C_3N_4/CS nanocomposite was synthesized by a self-assembly method. The Eg-C_3N_4/CS composite (1.0 g) was dispersed in 30 mL of distilled water while stirring for 30 min at room temperature. Ten milligrams of (0.01 M, 10 mL) $AgNO_3$ was mixed with the C_3N_4/CS composite solution while stirring at 30 min. Then, 0.25 M (10 mL) of $NaBH_4$ solution was added dropwise to obtain a dark gray solution and the formation of AgNPs on the Eg-C_3N_4/CS nanocomposite was confirmed. The AgNP/Eg-C_3N_4/CS nanocomposite was centrifuged with water and ethanol five times and dried in a hot air oven at 60 °C for 12 h, and the detailed mechanism is shown in Scheme 3.

4.6. Catalytic Reduction Method. Fifty milliliters of 20 ppm of $K_2Cr_2O_7$ in a 100 mL beaker and 1 mL of 2 mM formic acid (85%) were added to 15 mg of AgNP/Eg-C_3N_4/CS nanocomposite with stirring at 45 °C. Following the reaction, 2.5 mL of solution was taken at each time interval for monitoring the catalytic reduction efficiency of Cr(VI) to Cr(III) by a UV−visible spectrophotometer. The catalytic reduction of Cr(VI) to Cr(III) was also tested with other materials like Eg-C_3N_4/CS composites, CS, Eg-C_3N_4, and Bg-C_3N_4 under the same conditions. Additionally, sodium hydroxide (10 M, NaOH) was excessively added to the reduced (Cr(III)) solution, which appeared as a light green solution due to the reduction of Cr(VI) to Cr(III).

https://doi.org/10.1021/acsomega.1c00866
ACS Omega 2021, 6, 35221−35243

Scheme 3. Schematic Diagram of the Self-Assembled AgNP/Eg-C_3N_4/CS Nanocomposite

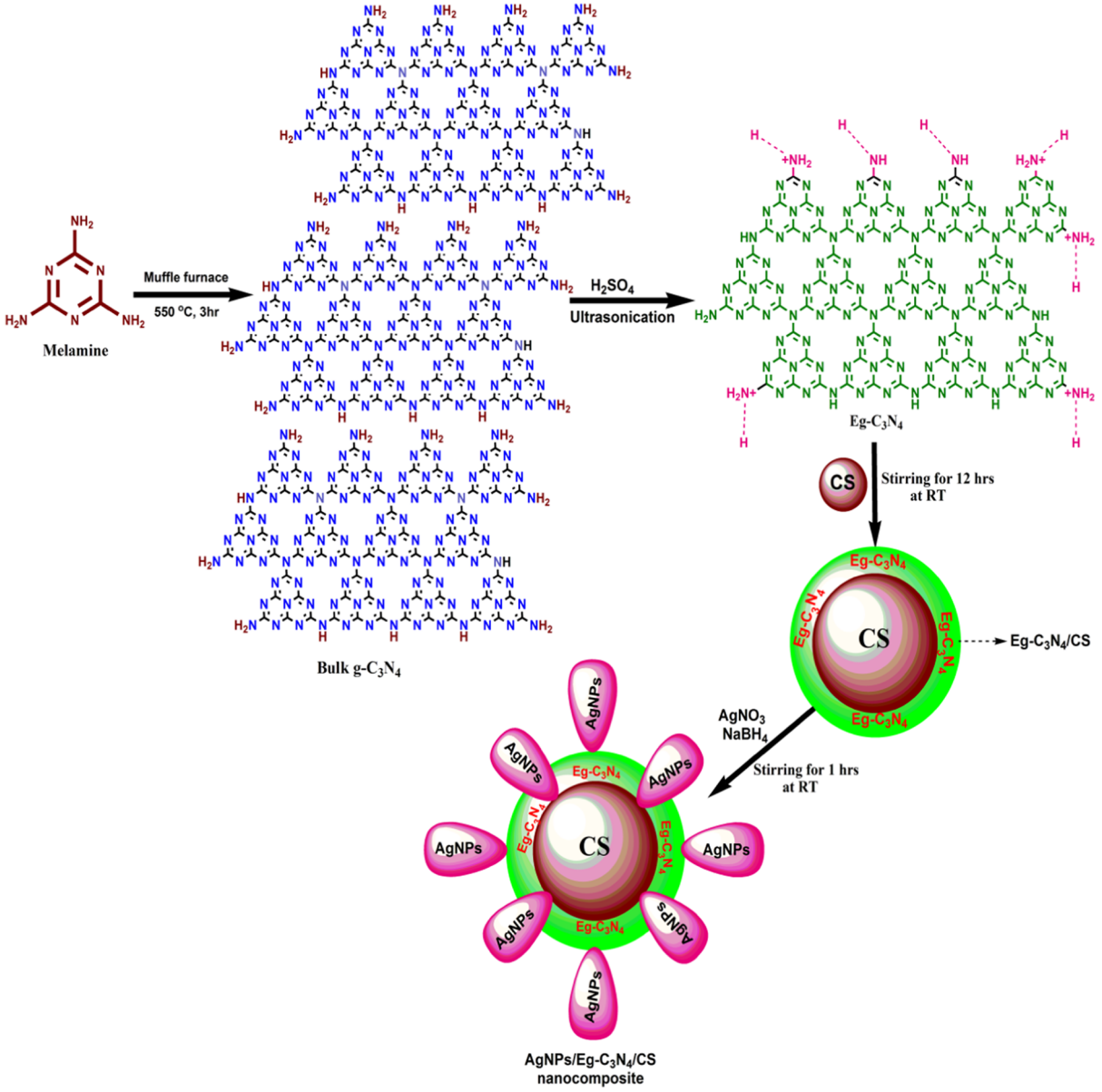

4.7. Catalytic Reduction Efficiency (%). The catalytic reduction efficiency α (%) of Cr(VI) to Cr(III) was calculated as given in eq 15.[186]

$$\text{reduction efficiency } \alpha\ (\%) = \frac{(C_I - C_F)}{C_F} \times 100 \quad (15)$$

where C_I is the initial concentration of reactants at t_I and C_F is the final concentration after reactants reacted with the catalyst at time t_F.

4.8. Turnover Frequency of the Heterogeneous Catalyst. The turnover frequency (TOF) is defined as the number of moles of reactants (Cr(VI)) reduced per mole of the AgNP/Eg-C_3N_4/CS nanocomposite catalyst sites per unit time. The TOF was investigated by following eq 16 with a unit of mol/mol × min.[187]

$$\text{TOF} = \text{TON/min} \quad (16)$$

where TON is equal to the number of moles of the reactant/number of moles of catalyst sites.

4.9. Characterization of Materials. The optical properties of Bg-C_3N_4, Eg-C_3N_4, CS, Eg-C_3N_4/CS, and AgNP/Eg-C_3N_4/CS nanocomposites were determined by a UV−visible spectrophotometer (Shimadzu UV-1208 model) and a fluorescence spectrometer (PerkinElmer spectrometer). Fourier transformation infrared (FT-IR) spectroscopy was used to investigate the functionalization of prepared materials by a PerkinElmer PE 1600, in the range of 4000−400 cm^{-1}, and KBr was also used to make the pellet. The crystalline nature of materials was investigated with a Philips PW1729 X-ray diffractometer, with Cu Kα radiation (λ = 1.5406 Å) working at 45 kV and 40 mA. Raman spectra were recorded with a PerkinElmer spectrometer and a laser excitation line of 532 nm. ζ potentials of Bg-C_3N_4, Eg-C_3N_4, CS, Eg-C_3N_4/CS, and AgNP/Eg-C_3N_4/CS nanocomposites were calculated using the surface charge with a Malvern Zetasizer NanoZS 90. The surface morphology of the prepared materials was also confirmed by a scanning electron microscope (TESCAN, VEGA SEM, electron acceleration voltage 20 kV). The sizes of Bg-C_3N_4, Eg-C_3N_4, Eg-

https://doi.org/10.1021/acsomega.1c00866
ACS Omega 2021, 6, 35221−35243

C_3N_4/CS, and AgNP/Eg-C_3N_4/CS nanocomposites were obtained by a transmission electron microscope (TEM JEOL JEM-2100F, electron accelerating voltage of 200 kV). Electrochemical impedance spectroscopy (EIS) was performed with a GAMRY electrochemical instrument (Interface 1000, potentiostat/galvanostat/ZRA, 11085, working electrode glassy carbon electrode (GCE), platinum wire auxiliary electrode, and Ag/AgCl reference electrode). The catalytic reduction of the $K_2Cr_2O_7$ solution was monitored using a UV−visible spectrophotometer (Shimadzu UV-1208 model), and the pH adjustment was conducted with an OHAUS starter 2100. The reuse application for the photocatalytic degradation of methylene blue with Cr(III)-AgNP/Eg-C_3N_4/CS was investigated by a 500 mL capacity glass quartz reactor and a 250 W xenon lamp as a visible light supply with filter glasses (λ > 420 nm).

4.10. Confirmation of Catalytic Reduction of Cr(VI) to Cr(III) by the DPC Method. Additionally, the catalytic reduction of Cr(VI) to Cr(III) over a period of time was determined by a spectrophotometric method with 1,5-diphenylcarbazide (DPC) using a Shimadzu UV-2550 double-beam UV−visible spectrophotometer with a 1 cm quartz cell at λ = 540 nm.[188] Cr(VI) was sensitively reacted with DPC to produce a reddish-violet complex. Then, the DPC method was used to perform for Cr(VI) after catalytic reduction for over a period of time, which did not change the color of solution, and this result confirmed the complete reduction of Cr(VI) to Cr(III).[189]

4.11. Reagents and Standard Procedures for the DPC Method. A 20 ppm solution was prepared by dilution of the standard stock solution of 1000 ppm $K_2Cr_2O_7$ in 50 mL of deionized water in a 100 mL beaker. One milliliter of 0.2 N H_2SO_4 was added to 100 mL of distilled water. 1,5-Diphenylcarbazide (0.25 g) was dissolved in 100 mL of acetonitrile, and 200 mL of distilled water was added. The standard solutions of Cr(VI) of 5, 10, 15, 20, and 25 ppm were prepared from the stock solution. The solution was maintained at pH 2 with dilute H_2SO_4 acid before the DPC test. The correlation coefficient R^2 = 0.999 was obtained from the absorbance vs concentration plot.

4.12. Scavenger Trapping Methods. The scavenger trapping methods were used to determine the active species in the photocatalytic degradation of MB. Isopropanol (IPA), *p*-benzoquinone (BQ), and ethylenediaminetetraacetic acid (EDTA) were used as scavengers for quenching $^{\bullet}OH$, $^{\bullet}O_2^-$, and h^+, respectively. This method was conducted during the photocatalytic degradation of MB by 1 mM scavengers.

■ ASSOCIATED CONTENT

Supporting Information

The Supporting Information is available free of charge at https://pubs.acs.org/doi/10.1021/acsomega.1c00866.

Raman spectra (Figure S1); N_2 adsorption−desorption isotherms (Figure S2); SEM images (Figure S3); fitting curves (Figures S4 and S5); UV−vis spectra (Figures S6 and S7); temperature study of catalytic reduction of Cr(VI) to Cr(III) (Figure S8); effect of pH on catalytic reduction of Cr(VI) to Cr(III) (Figure S9); mung bean seed germinate images (Figure S10); comparisons of photocatalytic degradation of MB with Cr(III)-AgNPs/Eg-C_3N_4/CS nanocomposite with other nanocomposites (Table S1) (PDF)

■ AUTHOR INFORMATION

Corresponding Author

Kriveshini Pillay − *Department of Chemical Sciences, University of Johannesburg, Johannesburg 2028, South Africa;* orcid.org/0000-0002-2134-7666; Phone: +27 115596128; Email: kriveshinip@uj.ac.za; Fax: +27 115596425

Author

Eswaran Prabakaran − *Department of Chemical Sciences, University of Johannesburg, Johannesburg 2028, South Africa*

Complete contact information is available at: https://pubs.acs.org/10.1021/acsomega.1c00866

Author Contributions

†E.P. and K.P. contributed to this work.

Notes

The authors declare no competing financial interest.

■ ACKNOWLEDGMENTS

This research was financially supported by the University of Johannesburg and the Faculty of Science, University of Johannesburg, South Africa. This research was also supported by the Center for Nanomaterials Research and the National Research Foundation (NRF).

■ REFERENCES

(1) Zhitkovich, A. Chromium in drinking water: sources, metabolism, and cancer risks. *Chem. Res. Toxicol.* **2011**, *24*, 1617−1629.

(2) Yadav, M.; Xu, Q. Catalytic chromium reduction using formic acid and metal nanoparticles immobilized in a metal−organic framework. *Chem Commun.* **2013**, *49*, 3327−3329.

(3) Stearns, D. M.; Kennedy, L. J.; Courtney, K. D.; Giangrande, P. H.; Phieffer, L. S.; Wetterhahn, K. E. Reduction of chromium (VI) by ascorbate leads to chromium-DNA binding and DNA strand breaks in vitro. *Biochemistry* **1995**, *34*, 910−919.

(4) Pradhan, D.; Sukla, L. B.; Sawyer, M.; Rahman, P. K. Recent bioreduction of hexavalent chromium in wastewater treatment: a review. *J. Ind. Eng. Chem.* **2017**, *55*, 1−20.

(5) Qin, F.; Wang, R.; Li, G.; Tian, F.; Zhao, H.; Chen, R. Highly efficient photocatalytic reduction of Cr (VI) by bismuth hollow nanospheres. *Catal. Commun.* **2013**, *42*, 14−19.

(6) Deveci, H.; Kar, Y. (2013). Adsorption of hexavalent chromium from aqueous solutions by bio-chars obtained during biomass pyrolysis. *J. Ind. Eng. Chem.* **2013**, *19*, 190−196.

(7) Padmavathy, K. S.; Madhu, G.; Haseena, P. V. A study on effects of pH, adsorbent dosage, time, initial concentration and adsorption isotherm study for the removal of hexavalent chromium (Cr (VI)) from wastewater by magnetite nanoparticles. *Procedia Technol.* **2016**, *24*, 585−594.

(8) Golestanifar, H. A. F. E. Z.; Haibati, B.; Amini, H.; Dehghani, M. H.; Asadi, A. Removal of hexavalent chromium from aqueous solution by adsorption on γ-alumina nanoparticles. *Environ. Prot. Eng.* **2015**, *41*, 133−145.

(9) Testa, J. J.; Grela, M. A.; Litter, M. I. Heterogeneous Photocatalytic Reduction of Chromium(VI) Over TiO_2 Particles in the Presence of Oxalate: Involvement of Cr(V) Species. *Environ. Sci. Technol.* **2004**, *38*, 1589−1594.

(10) Costa, M. Potential hazards of hexavalent chromate in our drinking water. *Toxicol. Appl. Pharmacol.* **2003**, *188*, 1−5.

(11) Kapil, V. *Chromium Toxicity*; U.S. Department of Health and Human Services, Public Health Services, Agency for Toxic Substances and Disease Registry: Atlanta, GA, 1990; pp 16−17.

(12) Wang, T.; Zhang, L.; Li, C.; Yang, W.; Song, T.; Tang, C.; Meng, Y.; Dai, S.; Wang, H.; Chai, L.; Luo, J. Synthesis of Core−Shell

Magnetic Fe_3O_4@Poly (m-Phenylenediamine) Particles for Chromium Reduction and Adsorption. *Environ. Sci. Technol.* **2015**, *49*, 5654−5662.
(13) Acharya, R.; Naik, B.; Parida, K. Cr (VI) remediation from aqueous environment through modified-TiO_2-mediated photocatalytic reduction. *Beilstein J. Nanotechnol.* **2018**, *9*, 1448−1470.
(14) Wu, J. H.; Shao, F. Q.; Luo, X. Q.; Xu, H. J.; Wang, A. J. Pd nanocones supported on g-C_3N_4: an efficient photocatalyst for boosting catalytic reduction of hexavalent chromium under visible-light irradiation. *Appl. Surf. Sci.* **2019**, *471*, 935−942.
(15) Richtera, L.; Nguyen, H. V.; Hynek, D.; Kudr, J.; Adam, V. Electrochemical Speciation Analysis for Simultaneous Determination of Cr(III) and Cr(VI) using an Activated Glassy Carbon Electrode. *Analyst* **2016**, *141*, 5577−5585.
(16) Xiao, K.; Han, G.; Li, J.; Dan, Z.; Xu, F.; Jiang, L.; Duan, N. Evaluation of Polyacrylic Anion Exchange Resins on the Removal of Cr(VI) from Aqueous Solutions. *RSC Adv.* **2016**, *6*, 5233−5239.
(17) Mane, C. P.; Mahamuni, S. V.; Kolekar, S. S.; Han, S. H.; Anuse, M. A. Hexavalent Chromium Recovery by Liquid−Liquid Extraction with 2-Octylaminopyridine from Acidic Chloride Media and its Sequential Separation from Other Heavy Toxic Metal Ions. *Arabian J. Chem.* **2016**, *9*, S1420−S1427.
(18) Li, H.; Li, Z.; Liu, T.; Xiao, X.; Peng, Z.; Deng, L. A novel technology for biosorption and recovery hexavalent chromium in wastewater by bio-functional magnetic beads. *Bioresour. Technol.* **2008**, *99*, 6271−6279.
(19) El-Taweel, Y. A.; Nassef, E. M.; Elkheriany, I.; Sayed, D. Removal of Cr(VI) Ions from Waste Water by Electrocoagulation using Iron Electrode. *Egypt. J. Pet.* **2015**, *24*, 183−192.
(20) Gheju, M.; Balcu, I. Removal of chromium from Cr (VI) polluted wastewaters by reduction with scrap iron and subsequent precipitation of resulted cations. *J. Hazard. Mater.* **2011**, *196*, 131−138.
(21) Wu, Q.; Zhao, J.; Qin, G.; Wang, C.; Tong, X.; Xue, S. Photocatalytic reduction of Cr (VI) with TiO_2 film under visible light. *Appl. Catal., B* **2013**, *142−143*, 142−148.
(22) Thornton, E. C.; Amonette, J. E. Hydrogen sulfide gas treatment of Cr (VI)-contaminated sediment samples from a plating-waste disposal site implications for in-situ remediation. *Environ. Sci. Technol.* **1999**, *33*, 4096−4101.
(23) Fruchter, J. S.; Cole, C. R.; Williams, M. D.; Vermeul, V. R.; Amonette, J. E.; Szecsody, J. E.; Istok, J. D.; Humphrey, M. D. Creation of a subsurface permeable treatment zone for aqueous chromate contamination using in situ redox manipulation. *Groundwater Monit. Rem.* **2000**, *20*, 66−77.
(24) Sedlak, D. L.; Chan, P. G. The reduction of Cr (VI) by Fe (II) in natural water. *Geochim. Cosmochim. Acta* **1997**, *61*, 2185−2192.
(25) Bao, S.; Liu, H.; Liu, Y.; Yang, W.; Wang, Y.; Yu, Y.; Sun, Y.; Li, K. Amino-functionalized graphene oxide-supported networked Pd−Ag nanowires as highly efficient catalyst for reducing Cr (VI) in industrial effluent by formic acid. *Chemosphere* **2020**, *257*, No. 27245.
(26) Wang, L.; Yamauchi, Y. Autoprogrammed synthesis of triple-layered Au@Pd@Pt core−shell nanoparticles consisting of a Au@Pd bimetallic core and nanoporous Pt shell. *J. Am. Chem. Soc.* **2010**, *132*, 13636−13638.
(27) Wang, D.; Li, Y. Bimetallic nanocrystals: liquid-phase synthesis and catalytic applications. *Adv. Mater.* **2011**, *23*, 1044−1060.
(28) Omole, M. A.; K'Owino, I. O.; Sadik, O. A. Palladium nanoparticles for catalytic reduction of Cr(VI) using formic acid. *Appl. Catal., B* **2007**, *76*, 158−167.
(29) Shao, F. Q.; Feng, J. J.; Lin, X. X.; Jiang, L. Y.; Wang, A. J. Simple fabrication of AuPd@ Pd core-shell nanocrystals for effective catalytic reduction of hexavalent chromium. *Appl. Catal., B* **2017**, *208*, 128−134.
(30) Gawande, M. B.; Goswami, A.; Asefa, T.; Guo, H.; Biradar, A. V.; Peng, D. L.; Zboril, R.; Varma, R. S. Core−shell nanoparticles: synthesis and applications in catalysis and electrocatalysis. *Chem. Soc. Rev.* **2015**, *44*, 7540−7590.
(31) Li, H. H.; Ma, S. Y.; Fu, Q. Q.; Liu, X. J.; Wu, L.; Yu, S. H. Scalable bromide-triggered synthesis of Pd@ Pt core−shell ultrathin nanowires with enhanced electrocatalytic performance toward oxygen reduction reaction. *J. Am. Chem. Soc.* **2015**, *137*, 7862−7868.
(32) Yang, C. W.; Chanda, K.; Lin, P. H.; Wang, Y. N.; Liao, C. W.; Huang, M. H. Fabrication of Au−Pd core−shell heterostructures with systematic shape evolution using octahedral nanocrystal cores and their catalytic activity. *J. Am. Chem. Soc.* **2011**, *133*, 19993−20000.
(33) Hu, L. Y.; Chen, L. X.; Liu, M. T.; Wang, A. J.; Wu, L. J.; Feng, J. J. Theophylline-assisted, eco-friendly synthesis of PtAu nanospheres at reduced graphene oxide with enhanced catalytic activity towards Cr (VI) reduction. *J. Colloid Interface Sci.* **2017**, *493*, 94−102.
(34) Yu, F.; Zhou, W.; Bellabarba, R. M.; Tooze, R. P. One-step synthesis and shape-control of CuPd nanowire networks. *Nanoscale* **2014**, *6*, 1093−1098.
(35) Niu, P.; Zhang, L.; Liu, G.; Cheng, H. M. Graphene-like carbon nitride nanosheets for improved photocatalytic activities. *Adv. Funct. Mater.* **2012**, *22*, 4763−4770.
(36) Yang, S.; Gong, Y.; Zhang, J.; Zhan, L.; Ma, L.; Vajtai, R.; Fang, Z.; Ajayan, P. M. Exfoliated graphitic carbon nitride nanosheets as efficient catalysts for hydrogen evolution under visible light. *Adv. Mater.* **2013**, *25*, 2452−2456.
(37) Zheng, Y.; Lin, L.; Wang, B.; Wang, X. Graphitic carbon nitride polymers toward sustainable photoredox catalysis. *Angew. Chem., Int. Ed.* **2015**, *54*, 12868−12884.
(38) Ni, Z.; Dong, F.; Huang, H.; Zhang, Y. New insights into how Pd nanoparticles influence the photocatalytic oxidation and reduction ability of gC_3N_4 nanosheets. *Catal. Sci. Technol.* **2016**, *6*, 6448−6458.
(39) Dong, F.; Zhao, Z.; Sun, Y.; Zhang, Y.; Yan, S.; Wu, Z. An advanced semimetal−organic Bi spheres−g-C_3N_4 nanohybrid with SPR-enhanced visible-light photocatalytic performance for NO purification. *Environ. Sci. Technol.* **2015**, *49*, 12432−12440.
(40) Wang, Y.; Wang, X.; Antonietti, M. Polymeric graphitic carbon nitride as a heterogeneous organocatalyst: from photochemistry to multipurpose catalysis to sustainable chemistry. *Angew. Chem., Int. Ed.* **2012**, *51*, 68−89.
(41) Liao, G.; Chen, S.; Quan, X.; Yu, H.; Zhao, H. Graphene oxide modified gC_3N_4 hybrid with enhanced photocatalytic capability under visible light irradiation. *J. Mater. Chem.* **2012**, *22*, 2721−2726.
(42) Ge, L.; Han, C. Synthesis of MWNTs/g-C_3N_4 composite photocatalysts with efficient visible light photocatalytic hydrogen evolution activity. *Appl. Catal., B* **2012**, *117−118*, 268−274.
(43) Ma, L.; Fan, H.; Fu, K.; Lei, S.; Hu, Q.; Huang, H.; He, G. Protonation of graphitic carbon nitride (g-C_3N_4) for an electrostatically self-assembling carbon@g-C_3N_4 core−shell nanostructure toward high hydrogen evolution. *ACS Sustainable Chem. Eng.* **2017**, *5*, 7093−7103.
(44) Fang, S.; Xia, Y.; Lv, K.; Li, Q.; Sun, J.; Li, M. Effect of carbon-dots modification on the structure and photocatalytic activity of g-C_3N_4. *Appl. Catal., B* **2016**, *185*, 225−232.
(45) Li, G.; Lian, Z.; Wang, W.; Zhang, D.; Li, H. Nanotube-confinement induced size-controllable g-C_3N_4 quantum dots modified single-crystalline TiO_2 nanotube arrays for stable synergetic photo-electrocatalysis. *Nano Energy* **2016**, *19*, 446−454.
(46) Chen, K.; Chai, Z.; Li, C.; Shi, L.; Liu, M.; Xie, Q.; Zhang, Y.; Xu, D.; Manivannan, A.; Liu, Z. Catalyst-free growth of three-dimensional graphene flakes and graphene/g-C_3N_4 composite for hydrocarbon oxidation. *ACS Nano* **2016**, *10*, 3665−3673.
(47) Celebi, M.; Karakas, K.; Ertas, I. E.; Kaya, M.; Zahmakiran, M. Palladium nanoparticles decorated graphene oxide: active and reusable nanocatalyst for the catalytic reduction of hexavalent chromium (VI). *ChemistrySelect* **2017**, *2*, 8312−8319.
(48) Veerakumar, P.; Thanasekaran, P.; Lin, K. C.; Liu, S. B. Biomass derived sheet-like carbon/palladium nanocomposite: an excellent opportunity for reduction of toxic hexavalent chromium. *ACS Sustainable Chem. Eng.* **2017**, *5*, 5302−5312.
(49) Kim, J. D.; Choi, H. C. Efficient catalytic reduction of hexavalent chromium with Pd-decorated carbon nanotubes. *Bull. Korean Chem. Soc.* **2016**, *37*, 744−747.
(50) Guo, Y.; Wang, D.; Liu, X.; Wang, X.; Liu, W.; Qin, W. Synthesis and characterization of the nickel@carbon dots hybrid material and its application in the reduction of Cr(VI). *New J. Chem.* **2014**, *38*, 5861−5867.

https://doi.org/10.1021/acsomega.1c00866
ACS Omega 2021, 6, 35221−35243

(51) Vellaichamy, B.; Periakaruppan, P. A Facile, One-pot and Ecofriendly Synthesis of Gold/Silver Nanobimetallics Smartened rGO for Enhanced Catalytic Reduction of Hexavalent Chromium. *RSC Adv.* **2016**, *6*, 57380−57388.
(52) Liu, L.; Xue, J.; Shan, X.; He, G.; Wang, X.; Chen, H. In-situ preparation of three-dimensional Ni@graphene-Cu composites for ultrafast reduction of Cr(VI) at room temperature. *Catal. Commun.* **2016**, *75*, 13−17.
(53) Celebi, M.; Yurderi, M.; Bulut, A.; Kaya, M.; Zahmakiran, M. Palladium nanoparticles supported on amine-functionalized SiO_2 for the catalytic hexavalent chromium reduction. *Appl. Catal., B* **2016**, *180*, 53−64.
(54) Vellaichamy, B.; Periakaruppan, P.; Nagulan, B. Reduction of Cr^{6+} from wastewater using a novel in situ-synthesized PANI/MnO_2/TiO_2 nanocomposite: renewable, selective, stable, and synergistic catalysis. *ACS Sustainable Chem. Eng.* **2017**, *5*, 9313−9324.
(55) Liang, M.; Su, R.; Qi, W.; Zhang, Y.; Huang, R.; Yu, Y.; Wang, L.; He, Z. Reduction of hexavalent chromium using recyclable Pt/Pd nanoparticles immobilized on procyanidin-grafted eggshell membrane. *Ind. Eng. Chem. Res.* **2014**, *53*, 13635−13643.
(56) Fu, G. T.; Jiang, X.; Wu, R.; Wei, S. H.; Sun, D. M.; Tang, Y. W.; Lu, T. H.; Chen, Y. Arginine-assisted synthesis and catalytic properties of single-crystalline palladium tetrapods. *ACS Appl. Mater. Interfaces* **2014**, *6*, 22790−22795.
(57) Han, S. H.; Liu, H. M.; Sun, C. C.; Jin, P. J.; Chen, Y. Photocatalytic performance of AgCl@Ag core−shell nanocubes for the hexavalent chromium reduction. *J. Mater. Sci.* **2018**, *53*, 12030−12039.
(58) Rakibuddin, M.; Ananthakrishnan, R. A novel Ag deposited nanocoordination polymer derived porous SnO_2/NiO heteronanostructure for the enhanced photocatalytic reduction of Cr(VI) under visible light. *New J. Chem.* **2016**, *40*, 3385−3394.
(59) Pawar, R. C.; Lee, C. S. Sensitization of CdS nanoparticles onto reduced graphene oxide (RGO) fabricated by chemical bath deposition method for effective removal of Cr(VI). *Mater. Chem. Phys.* **2013**, *141*, 686−693.
(60) Patnaik, S.; Das, K. K.; Mohanty, A.; Parida, K. Enhanced photo catalytic reduction of Cr (VI) over polymer-sensitized g-C_3N_4/$ZnFe_2O_4$ and its synergism with phenol oxidation under visible light irradiation. *Catal. Today.* **2018**, *315*, 52−66.
(61) Padhi, D. K.; Panigrahi, T. K.; Parida, K.; Singh, S. K.; Mishra, P. M. Green synthesis of Fe_3O_4/RGO nanocomposite with enhanced photocatalytic performance for Cr (VI) reduction, phenol degradation, and antibacterial activity. *ACS Sustainable Chem. Eng.* **2017**, *5*, 10551−10562.
(62) Nanda, B.; Pradhan, A. C.; Parida, K. M. Fabrication of mesoporous CuO/ZrO_2-MCM-41 nanocomposites for photocatalytic reduction of Cr (VI). *Chem. Eng. J.* **2017**, *316*, 1122−1135.
(63) Padhi, D. K.; Baral, A.; Parida, K.; Singh, S. K.; Ghosh, M. K. Visible light active single-crystal nanorod/needle-like α-MnO_2@RGO nanocomposites for efficient photoreduction of Cr (VI). *J. Phys. Chem. C.* **2017**, *121*, 6039−6049.
(64) Mishra, P. M.; Naik, G. K.; Nayak, A.; Parida, K. M. Facile synthesis of nano-structured magnetite in presence of natural surfactant for enhanced photocatalytic activity for water decomposition and Cr (VI) reduction. *Chem. Eng. J.* **2016**, *299*, 227−235.
(65) Padhi, D. K.; Parida, K. Facile fabrication of α-FeOOH nanorod/RGO composite: a robust photocatalyst for reduction of Cr(VI) under visible light irradiation. *J. Mater. Chem. A.* **2014**, *2*, 10300−10312.
(66) Kumar Padhi, D.; Pradhan, G. K.; Parida, K. M.; Singh, S. K. Facile fabrication of $Gd(OH)_3$ nanorod/RGO composite: synthesis, characterisation and photocatalytic reduction of Cr(VI). *Chem. Eng. J.* **2014**, *255*, 78−88.
(67) Mansingh, S.; Sultana, S.; Acharya, R.; Ghosh, M. K.; Parida, K. M. Efficient photon conversion via double charge dynamics CeO_2−$BiFeO_3$ p−n heterojunction photocatalyst promising toward N_2 fixation and phenol−Cr (VI) detoxification. *Inorg. Chem.* **2020**, *59*, 3856−3873.
(68) Kandi, D.; Martha, S.; Thirumurugan, A.; Parida, K. M. CdS QDs-decorated self-doped γ-Bi_2MoO_6: a sustainable and versatile photocatalyst toward photoreduction of Cr (VI) and degradation of phenol. *ACS Omega* **2017**, *2*, 9040−9056.
(69) Nayak, S.; Parida, K. M. Dynamics of Charge-Transfer Behavior in a Plasmon-Induced Quasi-Type-II p-n/n-n Dual Heterojunction in Ag@Ag_3PO_4/g-C_3N_4/NiFe LDH Nanocomposites for Photocatalytic Cr(VI) Reduction and Phenol Oxidation. *ACS Omega* **2018**, *3*, 7324−7343.
(70) Zhang, R.; Liu, H.; Wang, B.; Ling, L. Insights into the preference of CO_2 formation from HCOOH decomposition on Pd surface: a theoretical study. *J. Phys. Chem. C.* **2012**, *116*, 22266−22280.
(71) Tian, Y.; Tatsuma, T. Mechanisms and applications of plasmon-induced charge separation at TiO_2 films loaded with gold nanoparticles. *J. Am. Chem. Soc.* **2005**, *127*, 7632−7637.
(72) Wu, J. H.; Shao, F. Q.; Han, S. Y.; Bai, S.; Feng, J. J.; Li, Z.; Wang, A. J. Shape-controlled synthesis of well-dispersed platinum nanocubes supported on graphitic carbon nitride as advanced visible-light-driven catalyst for efficient photoreduction of hexavalent chromium. *J. Colloid Interface Sci.* **2019**, *535*, 41−49.
(73) Liang, Y. C.; Wang, C. C.; Kei, C. C.; Hsueh, Y. C.; Cho, W. H.; Perng, T. P. Photocatalysis of Ag-loaded TiO_2 nanotube arrays formed by atomic layer deposition. *J. Phys. Chem. C* **2011**, *115*, 9498−9502.
(74) Song, J.; Kim, H.; Jang, Y.; Jang, J. Enhanced antibacterial activity of silver/polyrhodanine-composite-decorated silica nanoparticles. *ACS Appl. Mater. Interfaces* **2013**, *5*, 11563−11568.
(75) Hirakawa, T.; Kamat, P. V. Charge separation and catalytic activity of Ag@TiO_2 core− shell composite clusters under UV−irradiation. *J. Am. Chem. Soc.* **2005**, *127*, 3928−3934.
(76) Song, Y.; Peng, Y.; Long, N. V.; Huang, Z.; Yang, Y. Multifunctional self-assembly 3D Ag/g-C_3N_4/RGO aerogel as highly efficient adsorbent and photocatalyst for R6G removal from wastewater. *Appl Surf Sci.* **2020**, *542*, No. 148584.
(77) Cheng, F.; Wang, H.; Dong, X. The amphoteric property of g-C_3N_4 nanosheets and its relevant heterostructure photocatalysts by an electrostatic re-assembly route. *Chem. Commun.* **2015**, *51*, 7176−7179.
(78) Cui, Y. J.; Zhang, J. S.; Zhang, G. G.; Huang, J. H.; Liu, P.; Antonietti, M.; Wang, X. C. Synthesis of bulk and nanoporous carbon nitridepolymers from ammonium thiocyanate for photocatalytic hydrogen evolution. *J. Mater. Chem.* **2011**, *21*, 13032−13039.
(79) Zhao, Y. C.; Liu, Z.; Chu, W. G.; Song, L.; Zhang, Z. X.; Yu, D. L.; Tian, Y. J.; Xie, S. S.; Sun, L. F. Large-scale synthesis of nitrogen-rich carbon nitride microfibers using graphitic carbon nitride as precursor. *Adv. Mater.* **2008**, *20*, 1777−1778.
(80) Yan, H.; Chen, Y.; Xu, S. Synthesis of graphitic carbon nitride by directly heating sulfuric acid treated melamine for enhanced photocatalytic H2 production from water under visible light. *Int. J. Hydrogen Energy* **2012**, *37*, 125−133.
(81) Xia, X.; Deng, N.; Cui, G.; Xie, J.; Shi, X.; Zhao, Y.; Wang, Q.; Wang, W.; Tang, B. NIR light induced H_2 evolution by a metal-free photocatalyst. *Chem. Commun.* **2015**, *51*, 10899.
(82) Zhang, W.; Zhou, L.; Deng, H. Ag modified g-C_3N_4 composites with enhanced visible-light photocatalytic activity for diclofenac degradation. *J. Mol. Catal. A: Chem.* **2016**, *423*, 270−276.
(83) Tang, S.; Vongehr, S.; Meng, X. K. Carbon Spheres with Controllable Silver Nanoparticle Doping. *J. Phys. Chem. C* **2010**, *114*, 977−982.
(84) Chen, L. L.; Zhang, W. X.; Feng, C.; Yang, Z. H.; Yang, Y. M. Replacement/etching route to ZnSe nanotube arrays and their enhanced photocatalytic activities. *Ind. Eng. Chem. Res.* **2012**, *51*, 4208−4214.
(85) Qi, K.; Li, Y.; Xie, Y.; Liu, S. Y.; Zheng, K.; Chen, Z.; Wang, R. Ag loading enhanced photocatalytic activity of g-C_3N_4 porous nanosheets for decomposition of organic pollutants. *Front. Chem.* **2019**, *7*, No. 91.
(86) Aghdam, S. M.; Haghighi, M.; Allahyari, S.; Yosefi, L. Precipitation dispersion of various ratios of BiOI/BiOCl nanocomposite over g-C_3N_4 for promoted visible light nanophotocatalyst used in removal of acid orange 7 from water. *J. Photochem. Photobiol., A* **2017**, *338*, 201−212.
(87) Qin, J.; Huo, J.; Zhang, P.; Zeng, J.; Wang, T.; Zeng, H. Improving the photocatalytic hydrogen production of Ag/gC_3N_4

https://doi.org/10.1021/acsomega.1c00866
ACS Omega 2021, 6, 35221−35243

nanocomposites by dye-sensitization under visible light irradiation. *Nanoscale* **2016**, *8*, 2249−2259.
(88) Sun, J. X.; Yuan, Y. P.; Qiu, L. G.; Jiang, X.; Xie, A. J.; Shen, Y. H.; Zhu, J. F. Fabrication of composite photocatalyst gC_3N_4−ZnO and enhancement of photocatalytic activity under visible light. *Dalton Trans.* **2012**, *41*, 6756−6763.
(89) Chen, Z.; Sun, P.; Fan, B.; Liu, Q.; Zhang, Z.; Fang, X. Textural and electronic structure engineering of carbon nitride via doping with π-deficient aromatic pyridine ring for improving photocatalytic activity. *Appl. Catal., B* **2015**, *170*−*171*, 10−16.
(90) Pattnaik, S. P.; Behera, A.; Martha, S.; Acharya, R.; Parida, K. Facile synthesis of exfoliated graphitic carbon nitride for photocatalytic degradation of ciprofloxacin under solar irradiation. *J. Mater. Sci.* **2019**, *54*, 5726−5742.
(91) Li, M.; Li, W.; Liu, S. Control of the morphology and chemical properties of carbon spheres prepared from glucose by a hydrothermal method. *J. Mater. Res.* **2012**, *27*, 1117−1123.
(92) Su, F. Z.; Mathew, S. C.; Lipner, G.; Fu, X. Z.; Antonietti, M.; Blechert, S.; Wang, X. C. mpg-C_3N_4-Catalyzed Selective Oxidation of Alcohols Using O_2 and Visible Light. *J. Am. Chem. Soc.* **2010**, *132*, 16299−16301.
(93) Ong, W. J.; Tan, L. L.; Chai, S. P.; Yong, S. T.; Mohamed, A. R. Surface charge modification via protonation of graphitic carbon nitride (g-C_3N_4) for electrostatic self-assembly construction of 2D/2D reduced graphene oxide (rGO)/g-C_3N_4 nanostructures toward enhanced photocatalytic reduction of carbon dioxide to methane. *Nano Energy* **2015**, *13*, 757−770.
(94) Song, H.; Huang, J.; Jia, X.; Sheng, W. Facile synthesis of core−shell Ag@C nanospheres with improved tribological properties for water-based additives. *New J. Chem.* **2018**, *42*, 8773−8782.
(95) Fina, F.; Callear, S. K.; Carins, G. M.; Irvine, J. T. S. Structural investigation of graphitic carbon nitride via XRD and neutron diffraction. *Chem. Mater.* **2015**, *27*, 2612−2618.
(96) Bai, X.; Wang, L.; Zong, R.; Zhu, Y. Photocatalytic activity enhanced via g-C_3N_4 nanoplates to nanorods. *J. Phys. Chem. C* **2013**, *117*, 9952−9961.
(97) Mi, Y.; Hu, W.; Dan, Y.; Liu, Y. Synthesis of carbon microspheres by a glucose hydrothermal method. *Mater. Lett.* **2008**, *62*, 1194−1196.
(98) Groenewolt, M.; Antonietti, M. Synthesis of g-C_3N_4 nanoparticles in mesoporous silica host matrices. *Adv. Mater.* **2005**, *17*, 1789−1792.
(99) Qi, F.; Li, Y.; Wang, Y.; Wang, Y.; Liu, S.; Zhao, X. Ag-Doped gC_3N_4 film electrode: Fabrication, characterization and photoelectron catalysis property. *RSC Adv.* **2016**, *6*, 81378−81385.
(100) Nagajyothi, P. C.; Pandurangan, M.; Vattikuti, S. V. P.; Tettey, C. O.; Sreekanth, T. V. M.; Shim, J. Enhanced photocatalytic activity of Ag/g-C_3N_4 composite. *Sep. Purif. Technol.* **2017**, *188*, 228−237.
(101) Tang, S.; Vongehr, S.; Meng, X. Carbon spheres with controllable silver nanoparticle doping. *J. Phys. Chem. C* **2010**, *114*, 977−982.
(102) Wang, X. J.; Liu, C.; Li, X. L.; Li, F. T.; Li, Y. P.; Zhao, J.; Liu, R. H. Construction of g-C_3N_4/Al_2O_3 hybrids via in-situ acidification and exfoliation with enhanced photocatalytic activity. *Appl. Surf. Sci.* **2017**, *394*, 340−350.
(103) Lu, Y.; Ji, C.; Li, Y.; Qu, R.; Sun, C.; Zhang, Y. Facile one-pot synthesis of C and g-C_3N_4 composites with enhanced photocatalytic activity using hydroxymethylated melamine as carbon source and soft template. *Mater. Lett.* **2018**, *211*, 78−81.
(104) Zuo, S.; Chen, Y.; Liu, W.; Yao, C.; Li, Y.; Ma, J.; Kong, Y.; Mao, H.; Li, Z.; Fu, Y. Polyaniline/gC_3N_4 composites as novel media for anticorrosion coatings. *J. Coat. Technol. Res.* **2017**, *14*, 1307−1314.
(105) Wang, J.; Cong, J.; Xu, H.; Wang, J.; Liu, H.; Liang, M.; Gao, J.; Ni, Q.; Yao, J. Facile gel-based morphological control of Ag/g-C_3N_4 porous nanofibers for photocatalytic hydrogen generation. *ACS Sustainable Chem. Eng.* **2017**, *5*, 10633−10639.
(106) Sheng, Z. H.; Shao, L.; Chen, J. J.; Bao, W. J.; Wang, F. B.; Xia, X. H. Catalyst-free synthesis of nitrogen-doped graphene via thermal annealing graphite oxide with melamine and its excellent electrocatalysis. *ACS Nano* **2011**, *5*, 4350−4358.
(107) Kang, Y.; Yang, Y.; Yin, L. C.; Kang, X.; Wang, L.; Liu, G.; Cheng, H. M. Selective breaking of hydrogen bonds of layered carbon nitride for visible light photocatalysis. *Adv. Mater.* **2016**, *28*, 6471−6477.
(108) Zinin, P. V.; Ming, L. C.; Sharma, S. K.; Khabashesku, V. N.; Liu, X. R.; Hong, S. M.; Endo, S.; Acosta, T. Ultraviolet and near-infrared Raman spectroscopy of graphitic C_3N_4 phase. *Chem. Phys. Lett.* **2009**, *472*, 69−73.
(109) Jürgens, B.; Irran, E.; Senker, J.; Kroll, P.; Muller, H.; Schnick, W. Melem (2,5,8-triamino-tri-s-triazine), an important intermediate during condensation of melamine rings to graphitic carbon nitride: synthesis, structure determination by X-ray powder diffraction, solid-state NMR, and theoretical studies. *J. Am. Chem. Soc.* **2003**, *125*, 10288−10300.
(110) Koglin, E.; Kip, B. J.; Meier, R. J. Adsorption and displacement of melamine at the Ag/electrolyte interface probed by surface-enhanced Raman microprobe spectroscopy. *J. Phys. Chem. B* **1996**, *100*, 5078−5089.
(111) Wang, H.; Zhang, X.; Xie, J.; Zhang, J.; Ma, P.; Pan, B.; Xie, Y. Structural distortion in graphitic-C_3N_4 realizing an efficient photoreactivity. *Nanoscale* **2015**, *7*, 5152−5156.
(112) Wang, H.; Dai, Q.; Li, Q.; Yang, J.; Zhong, X.; Huang, Y.; Zhang, A.; Yan, Z. Preparation of porous carbon spheres from porous starch. *Solid State Ionics* **2009**, *180*, 1429−1432.
(113) Lu, J.; Yang, J. X.; Wang, J.; Lim, A.; Wang, S.; Loh, K. P. One-pot synthesis of fluorescent carbon nanoribbons, nanoparticles, and graphene by the exfoliation of graphite in ionic liquids. *ACS Nano* **2009**, *3*, 2367−2375.
(114) Ji, T.; Chen, L.; Schmitz, M.; Bao, F. S.; Zhu, J. Hierarchical macrotube/mesopore carbon decorated with mono-dispersed Ag nanoparticles as a highly active catalyst. *Green Chem.* **2015**, *17*, 2515−2523.
(115) Jiang, P.; Liu, J.; Huang, Y.; Jiang, X.; Lu, L. Study of Preparation, Growth Mechanism and Catalytic Performance of Carbon Based Embedded Silver Nano Composite Materials. *Eurasian Chem.-Technol. J.* **2017**, *19*, 17−22.
(116) Sing, K. S. Reporting physisorption data for gas/solid systems with special reference to the determination of surface area and porosity (Recommendations 1984). *Pure Appl. Chem.* **1985**, *57*, 603−619.
(117) Wang, F. L.; Pang, L. L.; Jiang, Y. Y.; Chen, B.; Lin, D.; Lun, N.; Zhu, H. L.; Liu, R.; Meng, X. L.; Wang, Y.; et al. Simple synthesis of hollow carbon spheres from glucose. *Mater. Lett.* **2009**, *63*, 2564−2566.
(118) Su, Q.; Sun, J.; Wang, J.; Yang, Z.; Cheng, W.; Zhang, S. Urea-derived graphitic carbon nitride as an efficient heterogeneous catalyst for CO_2 conversion into cyclic carbonates. *Catal. Sci. Technol.* **2014**, *4*, 1556−1562.
(119) Sun, Y.; Xiong, T.; Ni, Z.; Liu, J.; Dong, F.; Zhang, W.; Ho, W. K. Improving g-C_3N_4 photocatalysis for NOx removal by Ag nanoparticles decoration. *Appl. Surf. Sci.* **2015**, *358*, 356−362.
(120) Li, H.; Jing, Y.; Ma, X.; Liu, T.; Yang, L.; Liu, B.; Yin, S.; Wei, Y.; Wang, Y. Construction of a well-dispersed Ag/graphene-like gC_3N_4 photocatalyst and enhanced visible light photocatalytic activity. *RSC Adv.* **2017**, *7*, 8688−8693.
(121) Xu, J.; Li, Y.; Peng, S.; Lu, G.; Li, S. Eosin Y-sensitized graphitic carbon nitride fabricated by heating urea for visible light photocatalytic hydrogen evolution: The effect of the pyrolysis temperature of urea. *Phys. Chem. Chem. Phys.* **2013**, *15*, 7657−7665.
(122) Yu, Z.; Li, F.; Yang, Q.; Shi, H.; Chen, Q.; Xu, M. Nature-mimic method to fabricate polydopamine/graphitic carbon nitride for enhancing photocatalytic degradation performance. *ACS Sustainable Chem. Eng.* **2017**, *5*, 7840−7850.
(123) Hu, S.; Zhang, W.; Bai, J.; Lu, G.; Zhang, L.; Wu, G. Construction of a 2D/2D gC 3 N 4/rGO hybrid heterojunction catalyst with outstanding charge separation ability and nitrogen photofixation performance via a surface protonation process. *RSC Adv.* **2016**, *6*, 25695−25702.

https://doi.org/10.1021/acsomega.1c00866
ACS Omega 2021, 6, 35221−35243

(124) Wu, Y.; Zhou, Y.; Xu, H.; Liu, Q.; Li, Y.; Zhang, L.; Liu, H.; Tu, Z.; Cheng, X.; Yang, J. Highly active, superstable, and biocompatible Ag/polydopamine/g-C_3N_4 bactericidal photocatalyst: synthesis, characterization, and mechanism. *ACS Sustainable Chem. Eng.* **2018**, *6*, 14082−14094.
(125) Hou, Y.; Zuo, F.; Dagg, A.; Feng, P. A Three-Dimensional Branched Cobalt-Doped α-Fe_2O_3 Nanorod/$MgFe_2O_4$ Heterojunction Array as a Flexible Photoanode for Efficient Photoelectrochemical Water Oxidation. *Angew. Chem., Int. Ed.* **2013**, *52*, 1248−1252.
(126) Wu, M.; Gong, Y.; Nie, T.; Zhang, J.; Wang, R.; Wang, H.; He, B. Template-free synthesis of nanocage-like g-C_3N_4 with high surface area and nitrogen defects for enhanced photocatalytic H_2 activity. *J. Mater. Chem. A* **2019**, *7*, 5324−5332.
(127) Shi, A.; Li, H.; Yin, S.; Liu, B.; Zhang, J.; Wang, Y. Effect of conjugation degree and delocalized π-system on the photocatalytic activity of single layer g-C_3N_4. *Appl. Catal., B* **2017**, *218*, 137−146.
(128) Huang, R. L.; Huang, W. Q.; Li, D. F.; Ma, L. L.; Pan, A.; Hu, W.; Fan, X.; Huang, G. F. Self-assembled hierarchical carbon/g-C_3N_4 composite with high photocatalytic activity. *J. Phys. D: Appl. Phys.* **2018**, *51*, No. 135501.
(129) Wang, S.; Li, D.; Sun, C.; Yang, S.; Guan, Y.; He, H. Synthesis and characterization of g-C_3N_4/Ag_3VO_4 composites with significantly enhanced visible-light photocatalytic activity for triphenylmethane dye degradation. *Appl. Catal., B* **2014**, *144*, 885−892.
(130) Martha, S.; Nashim, A.; Parida, K. M. Facile synthesis of highly active g-C_3N_4 for efficient hydrogen production under visible light. *J. Mater. Chem. A* **2013**, *1*, 7816−7824.
(131) Hou, Y.; Wen, Z.; Cui, S.; Guo, X.; Chen, J. Constructing 2D porous graphitic C_3N_4 nanosheets/nitrogen-doped graphene/layered MoS_2 ternary nanojunction with enhanced photoelectrochemical activity. *Adv. Mater.* **2013**, *25*, 6291−6297.
(132) Liang, Q.; Li, Z.; Huang, Z. H.; Kang, F.; Yang, Q. H. Holey graphitic carbon nitride nanosheets with carbon vacancies for highly improved photocatalytic hydrogen production. *Adv. Funct. Mater.* **2015**, *25*, 6885−6892.
(133) Cui, Y.; Ding, Z.; Fu, X.; Wang, X. Construction of conjugated carbon nitride nanoarchitectures in solution at low temperatures for photoredox catalysis. *Angew. Chem.* **2012**, *124*, 11984−11988.
(134) Tang, S.; Vongehr, S.; Meng, X. Carbon spheres with controllable silver nanoparticle doping. *J. Phys. Chem. C* **2010**, *114*, 977−982.
(135) Chlistunoff, J. B.; Johnston, K. P. UV-Vis Spectroscopic Determination of the Dissociation Constant of Bichromate from 160 to 400 °C. *J. Phys. Chem. B* **1998**, *102*, 3993−4003.
(136) Balakumar, V.; Prakash, P. A Facile in-situ Synthesis of Highly Active and Reusable Ternary Ag-PPy-GO Nanocomposite for Catalytic Oxidation of Hydroquinone in Aqueous Solution. *J. Catal.* **2016**, *344*, 795−805.
(137) Li, H.; Wu, T.; Cai, B.; Ma, W.; Sun, Y.; Gan, S.; Han, D.; Niu, L. Efficiently photocatalytic reduction of carcinogenic contaminant Cr (VI) upon robust AgCl: Ag hollow nanocrystals. *Appl. Catal., B* **2015**, *164*, 344−351.
(138) Vellaichamy, B.; Periakaruppan, P. Catalytic Hydrogenation Performance of in-Situ Assembled Au@g-C_3N_4-PANI Nanoblend: Synergistic Inter-constituent Interactions Boost the Catalysis. *New J. Chem.* **2017**, *41*, 7123.
(139) Qamar, M.; Gondal, M. A.; Yamani, Z. H. Synthesis of Nanostructured NiO and Its Application in Laser-Induced Photocatalytic Reduction of Cr(VI) from Water. *J. Mol. Catal. A: Chem.* **2011**, *341*, 83−88.
(140) Marinho, B. A.; Cristóvão, R. O.; Djellabi, R.; Loureiro, J. M.; Boaventura, R. A. R.; Vilar, V. J. P. Photocatalytic Reduction of Cr(VI) Over TiO_2-coated Cellulose Acetate Monolithic Structures using Solar Light. *Appl. Catal., B* **2017**, *203*, 18−30.
(141) Li, S.; Tang, L.; Zeng, G.; Wang, J.; Deng, Y.; Wang, J.; Xie, Z.; Zhou, Y. Catalytic reduction of hexavalent chromium by a novel nitrogen-functionalized magnetic ordered mesoporous carbon doped with Pd nanoparticles. *Environ. Sci. Pollut. Res.* **2016**, *23*, 22027−22036.
(142) Xu, T.; Xue, J.; Zhang, X.; He, G.; Chen, H. Ultrafine cobalt nanoparticles supported on reduced graphene oxide: Efficient catalyst for fast reduction of hexavalent chromium at room temperature. *Appl. Surf. Sci.* **2017**, *402*, 294−300.
(143) Zhang, X.; Shang, N.; Zhou, X.; Feng, C.; Gao, S.; Wu, Q.; Wang, Z.; Wang, C. AgPd-MnOx Supported on Carbon Nanospheres: An Efficient Catalyst for Dehydrogenation of Formic Acid. *New J. Chem.* **2017**, *41*, 3443−3449.
(144) Li, S.; Ping, Y.; Yan, J.-M.; Wang, H.-L.; Wu, M.; Jiang, Q. Facile Synthesis of AgAuPd/Graphene with High Performance for Hydrogen Generation from Formic Acid. *J. Mater. Chem. A* **2015**, *3*, 14535−14538.
(145) Wang, Z. L.; Yan, J. M.; Wang, H. L.; Ping, Y.; Jiang, Q. Au@Pd Core-shell Nanoclusters Growing on Nitrogen-Doped Mildly Reduced Graphene Oxide with Enhanced Catalytic Performance for Hydrogen Generation from Formic Acid. *J. Mater. Chem. A* **2013**, *1*, 12721−12725.
(146) Gan, C.; Liu, Y.; Tan, X.; Wang, S.; Zeng, G.; Zheng, B.; Li, T.; Jiang, Z.; Liu, W. Effect of porous zinc−biochar nanocomposites on Cr (VI) adsorption from aqueous solution. *RSC Adv.* **2015**, *5*, 35107−35115.
(147) Bao, S.; Yang, W.; Wang, Y.; Yu, Y.; Sun, Y.; Li, K. PEI grafted amino-functionalized graphene oxide nanosheets for ultrafast and high selectivity removal of Cr (VI) from aqueous solutions by adsorption combined with reduction: Behaviors and mechanisms. *Chem. Eng. J.* **2020**, *399*, No. 125762.
(148) Jin, X.; Wang, H.; Jin, X.; Wang, H.; Chen, L.; Wang, W.; Lin, T.; Zhu, Z. Preparation of keratin/PET nanofiber membrane and its high adsorption performance of Cr (VI). *Sci. Total Environ.* **2020**, *710*, No. 135546.
(149) Avila, M.; Burks, T.; Akhtar, F.; Göthelid, M.; Lansaker, P. C.; Toprak, M. S.; Muhammed, M.; Uheida, A. Surface Functionalized Nanofibers for the Removal of Chromium(VI) from Aqueous Solutions. *Chem. Eng. J.* **2014**, *245*, 201−209.
(150) Huang, W.; Liu, N.; Zhang, X.; Wu, M.; Tang, L. Metal organic framework g-C_3N_4/MIL-53 (Fe) heterojunctions with enhanced photocatalytic activity for Cr (VI) reduction under visible light. *Appl. Surf. Sci.* **2017**, *425*, 107−116.
(151) Sanchez-Hachair, A.; Hofmann, A. Hexavalent chromium quantification in solution: comparing direct UV−visible spectrometry with 1, 5-diphenylcarbazide colorimetry. *C. R. Chim.* **2018**, *21*, 890−896.
(152) Zhao, J.; Li, Z.; Wang, J.; Li, Q.; Wang, X. Capsular Polypyrrole Hollow Nanofibers: An Efficient Recyclable Adsorbent for Hexavalent Chromium Removal. *J. Mater. Chem. A* **2015**, *3*, 15124−15132.
(153) Gao, Y.; Chen, C.; Tan, X.; Xu, H.; Zhu, K. Polyaniline-Modified 3D-Flower-like Molybdenum Disulfide Composite for Efficient Adsorption/Photocatalytic Reduction of Cr(VI). *J. Colloid Interface Sci.* **2016**, *476*, 62−70.
(154) Liu, S. X. Removal of copper (VI) from aqueous solution by Ag/TiO_2 photocatalysis. *Bull. Environ. Contam. Toxicol.* **2005**, *74*, 706−714.
(155) Burgess, W. A.; Tapriyal, D.; Gamwo, I. K.; Wu, Y.; McHugh, M. A.; Enick, R. M. New group-contribution parameters for the calculation of PC-SAFT parameters for use at pressures to 276 MPa and temperatures to 533 K. *Ind. Eng. Chem. Res.* **2014**, *53*, 2520−2528.
(156) Han, S. H.; Bai, J.; Liu, H. M.; Zeng, J. H.; Jiang, J. X.; Chen, Y.; Lee, J. M. One-pot fabrication of hollow and porous Pd−Cu alloy nanospheres and their remarkably improved catalytic performance for hexavalent chromium reduction. *ACS Appl. Mater. Interfaces* **2016**, *8*, 30948−30955.
(157) Grasemann, M.; Laurenczy, G. Formic acid as a hydrogen source-recent developments and future trends. *Energy Environ. Sci.* **2012**, *5*, 8171−8181.
(158) Mellmann, D.; Sponholz, P.; Junge, H.; Beller, M. Formic acid as a hydrogen storage material-development of homogeneous catalysts for selective hydrogen release. *Chem. Soc. Rev.* **2016**, *45*, 3954−3988.
(159) Zhang, S.; Metin, Ö.; Su, D.; Sun, S. Monodisperse AgPd alloy nanoparticles and their superior catalysis for the dehydrogenation of formic acid. *Angew. Chem., Int. Ed.* **2013**, *52*, 3681−3684.

https://doi.org/10.1021/acsomega.1c00866
ACS Omega 2021, 6, 35221−35243

(160) Gong, K.; Wang, W.; Yan, J.; Han, Z. Highly reduced molybdophosphate as a noble metal-free catalyst for the reduction of chromium using formic acid as a reducing agent. *J. Mater. Chem. A* **2015**, *3*, 6019−6027.
(161) Mori, K.; Dojo, M.; Yamashita, H. Pd−Ag Nanoparticles within a Macro Reticular Basic Resin: An Efficient Catalyst for Hydrogen Production from Formic Acid Decomposition. *ACS Catal.* **2013**, *3*, 1114−1119.
(162) Zhou, J.; Zhou, X.; Li, L.; Chen, Q. Enhanced liquid phase catalytic hydrogenation reduction of bromate over Pd-on-Au bimetallic catalysts. *Appl. Catal., A* **2018**, *562*, 142−149.
(163) Bhowmik, K.; Mukherjee, A.; Mishra, M. K.; De, G. Stable Ni nanoparticle-reduced graphene oxide composites for the reduction of highly toxic aqueous Cr(VI) at room temperature. *Langmuir* **2014**, *30*, 3209−3216.
(164) Huo, Y.; Wang, Z.; Zhang, J.; Liang, C.; Dai, K. Ag SPR-promoted 2D porous g-C_3N_4/Ag_2MoO_4 composites for enhanced photocatalytic performance towards methylene blue degradation. *Appl. Surf. Sci.* **2018**, *459*, 271−280.
(165) Singhal, S.; Dixit, S.; Shukla, A. K. Self-assembly of the Ag deposited ZnO/carbon nanospheres: a resourceful photocatalyst for efficient photocatalytic degradation of methylene blue dye in water. *Adv. Powder Technol.* **2018**, *29*, 3483−3492.
(166) Arif, M.; Li, Q.; Yao, J.; Huang, T.; Hua, Y.; Liu, T.; Liu, X. Enhance photocatalysis performance and mechanism of CdS and Ag synergistic co-catalyst supported on mesoporous g-C_3N_4 nanosheets under visible-light irradiation. *J. Environ. Chem. Eng.* **2017**, *5*, 5358−5368.
(167) Fu, Y.; Huang, T.; Zhang, L.; Zhu, J.; Wang, X. Ag/gC_3N_4 catalyst with superior catalytic performance for the degradation of dyes: a borohydride-generated superoxide radical approach. *Nanoscale* **2015**, *7*, 13723−13733.
(168) Ravichandran, K.; Sindhuja, E. Fabrication of cost effective g-C_3N_4+Ag activated ZnO photocatalyst in thin film form for enhanced visible light responsive dye degradation. *Mater. Chem. Phys.* **2019**, *221*, 203−215.
(169) Chen, Z.; Li, Y.; Guo, M.; Xu, F.; Peng Wang, P.; Du, Y.; Na, P. One-pot synthesis of Mn-doped TiO_2 grown on graphene and the mechanism for removal of Cr(VI) and Cr(III). *J. Hazard. Mater.* **2016**, *310*, 188−198.
(170) Umejuru, E. C.; Prabakaran, E.; Pillay, K. Coal fly ash coated with carbon hybrid nanocomposite for remediation of cadmium (II) and photocatalytic application of the spent adsorbent for reuse. *Results Mater.* **2020**, *7*, No. 100117.
(171) Gong, Y.; Quan, X.; Yu, H.; Chen, S. Synthesis of Z-scheme Ag_2CrO_4/Ag/g-C_3N_4 composite with enhanced visible-light photocatalytic activity for 2, 4-dichlorophenol degradation. *Appl. Catal., B* **2017**, *219*, 439−449.
(172) Sang, N. X.; Quan, N. M.; Tho, N. H.; Tuan, N. T.; Tung, T. T. Mechanism of enhanced photocatalytic activity of Cr-doped ZnO nanoparticles revealed by photoluminescence emission and electron spin resonance. *Semicond. Sci. Technol.* **2019**, *34*, No. 025013.
(173) Qamar, M. A.; Shahid, S.; Javed, M.; Iqbal, S.; Sher, M.; Akbar, M. B. Highly efficient g-C_3N_4/Cr-ZnO nanocomposites with superior photocatalytic and antibacterial activity. *J. Photochem. Photobiol., A* **2020**, *401*, No. 112776.
(174) Xue, J.; Ma, S.; Zhou, Y.; Zhang, Z.; Jiang, P. Synthesis of Ag/ZnO/C plasmonic photocatalyst with enhanced adsorption capacity and photocatalytic activity to antibiotics. *RSC Adv.* **2015**, *5*, 18832−18840.
(175) Liu, R.; Ping, W.; Xuefei, W.; Huogen, Y.; Jiaguo, Y. UV- and Visible-Light Photocatalytic Activity of Simultaneously Deposited and Doped Ag/Ag(I)-TiO_2 Photocatalyst. *J. Phys. Chem. C* **2012**, *116*, 17721−17728.
(176) Velo-Gala, I.; López-Peñalver, J. J.; Sánchez-Polo, M.; Rivera-Utrilla, J. Activated carbon as photocatalyst of reactions in aqueous phase. *Appl. Catal., B* **2013**, *142−143*, 694−704.
(177) Priya, A.; Arumugam, M.; Arunachalam, P.; Al-Mayouf, A. M.; Madhavan, J.; Theerthagiri, J.; Choi, M. Y. Fabrication of visible-light active BiFeWO6/ZnO nanocomposites with enhanced photocatalytic activity. *Colloids Surf., A* **2020**, *586*, No. 124294.
(178) Habib, I. Y.; Burhan, J.; Jaladi, F.; Lim, C. M.; Usman, A.; Kumara, N. T.; Tsang, S. C.; Mahadi, A. H. Effect of Cr doping in CeO_2 nanostructures on photocatalysis and H_2O_2 assisted methylene blue dye degradation. *Catal. Today* **2020**, DOI: 10.1016/j.cattod.2020.04.008.
(179) Kamal, S.; Balu, S.; Palanisamy, S.; Uma, K.; Velusamy, V.; Yang, T. C. Synthesis of boron doped C_3N_4/$NiFe_2O_4$ nanocomposite: An enhanced visible light photocatalyst for the degradation of methylene blue. *Results Phys.* **2019**, *12*, 1238−1244.
(180) Yu, H.; Huang, B.; Wang, H.; Yuan, X.; Jiang, L.; Wu, Z.; Zhang, J.; Zeng, G. Facile construction of novel direct solid-state Z-scheme AgI/BiOBr photocatalysts for highly effective removal of ciprofloxacin under visible light exposure: mineralization efficiency and mechanisms. *J. Colloid Interface Sci.* **2018**, *522*, 82−94.
(181) Shao, B. B.; Liu, Z. F.; Zeng, G. M.; Wu, Z. B.; Liu, Y.; Cheng, M.; Chen, M.; Liu, Y.; Zhang, W.; Feng, H. Nitrogen-doped hollow mesoporous carbon spheres modified g-C_3N_4/Bi_2O_3 direct dual semiconductor photocatalytic system with enhanced antibiotics degradation under visible light. *ACS Sustainable Chem. Eng.* **2018**, *6*, 16424−16436.
(182) Chen, F.; Yang, Q.; Wang, S.; Yao, F.; Sun, J.; Wang, Y.; Zhang, C.; Li, X.; Niu, C.; Wang, D.; Zeng, G. Graphene oxide and carbon nitride nanosheets co-modified silver chromate nanoparticles with enhanced visible-light photoactivity and anti-photocorrosion properties towards multiple refractory pollutants degradation. *Appl. Catal., B* **2017**, *209*, 493−505.
(183) Zeng, C.; Hu, Y.; Guo, Y.; Zhang, T.; Dong, F.; Du, X.; Zhang, Y.; Huang, H. Achieving tunable photocatalytic activity enhancement by elaborately engineering composition-adjustable polynary heterojunctions photocatalysts. *Appl. Catal., B* **2016**, *194*, 62−73.
(184) Watanabe, T.; Takizawa, T.; Honda, K. Photocatalysis through excitation of adsorbates.1. Highly efficient N-deethylation of Rhodamine B adsorbed to cadmium sulfide. *J. Phys. Chem. A* **1977**, *81*, 1845−1851.
(185) Prabakaran, E.; Pillay, K. A novel approach of fluorescent porous graphite carbon nitride based silica gel powder for latent fingerprint detection. *Appl. Nanosci.* **2019**, *9*, 255−277.
(186) Veerakumar, P.; Dhenadhayalan, N.; Lin, K. C.; Liu, S. B. Highly stable ruthenium nanoparticles on 3D mesoporous carbon: an excellent opportunity for reduction reactions. *J. Mater. Chem. A* **2015**, *3*, 23448−23457.
(187) Wei, L. L.; Gu, R.; Lee, J. M. Highly efficient reduction of hexavalent chromium on amino-functionalized palladium nanowires. *Appl. Catal., B* **2015**, *176−177*, 325−330.
(188) Clesceri, L. S.; Greenberg, A. E.; Eaton, A. D. *Standard Methods for the Examination of Water and Wastewater*, 20th ed.; American Public Health Association, American Water Work Association, and Water Environment Federation: Washington, DC, 1998; pp 366−368.
(189) Kostas, V.; Baikousi, M.; Dimos, K.; Vasilopoulos, K. C.; Koutselas, I.; Karakassides, M. A. Efficient and Rapid Photocatalytic Reduction of Hexavalent Chromium Achieved by a Phloroglucinol Derived Microporous Polymeric Organic Framework Solid. *J. Phys. Chem. C* **2017**, *121*, 7303−7311.

https://doi.org/10.1021/acsomega.1c00866
ACS Omega 2021, 6, 35221−35243